

# Emulating galaxy clustering and galaxy–galaxy lensing into the deeply non-linear regime: methodology, information, and forecasts

Benjamin D. Wibking<sup>Ⓧ</sup>,<sup>1</sup>★ Andrés N. Salcedo,<sup>1</sup> David H. Weinberg,<sup>1</sup>  
Lehman H. Garrison,<sup>2</sup> Douglas Ferrer,<sup>2</sup> Jeremy Tinker,<sup>3</sup> Daniel Eisenstein,<sup>2</sup>  
Marc Metchnik<sup>4</sup> and Philip Pinto<sup>4</sup>

<sup>1</sup>Department of Astronomy and Center for Cosmology and AstroParticle Physics, Ohio State University, 140 W 18th Ave, Columbus, OH, USA 43210

<sup>2</sup>Harvard-Smithsonian Center for Astrophysics, 60 Garden St., MS-10, Cambridge, MA 02138, USA

<sup>3</sup>Center for Cosmology and Particle Physics, New York University, 4 Washington Place, New York, NY 10003, USA

<sup>4</sup>Steward Observatory, University of Arizona, 933 N. Cherry Ave., Tucson, AZ 85121, USA

Accepted 2018 August 14. Received 2018 July 23; in original form 2017 September 23

## ABSTRACT

The combination of galaxy–galaxy lensing (GGL) with galaxy clustering is one of the most promising routes to determining the amplitude of matter clustering at low redshifts. We show that extending clustering+GGL analyses from the linear regime down to  $\sim 0.5 h^{-1}$  Mpc scales increases their constraining power considerably, even after marginalizing over a flexible model of non-linear galaxy bias. Using a grid of cosmological  $N$ -body simulations, we construct a Taylor-expansion emulator that predicts the galaxy autocorrelation  $\xi_{gg}(r)$  and galaxy-matter cross-correlation  $\xi_{gm}(r)$  as a function of  $\sigma_8$ ,  $\Omega_m$ , and halo occupation distribution (HOD) parameters, which are allowed to vary with large-scale environment to represent possible effects of galaxy assembly bias. We present forecasts for a fiducial case that corresponds to BOSS LOWZ galaxy clustering and SDSS-depth weak lensing (effective source density  $\sim 0.3 \text{ arcmin}^{-2}$ ). Using tangential shear and projected correlation function measurements over  $0.5 \leq r_p \leq 30 h^{-1}$  Mpc yields a 2 per cent constraint on the parameter combination  $\sigma_8 \Omega_m^{0.6}$ , a factor of two better than a constraint that excludes non-linear scales ( $r_p > 2 h^{-1}$  Mpc,  $4 h^{-1}$  Mpc for  $\gamma_t, w_p$ ). Much of this improvement comes from the non-linear clustering information, which breaks degeneracies among HOD parameters. Increasing the effective source density to  $3 \text{ arcmin}^{-2}$  sharpens the constraint on  $\sigma_8 \Omega_m^{0.6}$  by a further factor of two. With robust modelling into the non-linear regime, low-redshift measurements of matter clustering at the 1-per cent level with clustering+GGL alone are well within reach of current data sets such as those provided by the Dark Energy Survey.

**Key words:** gravitational lensing: weak – cosmological parameters – large-scale structure of Universe.

## 1 INTRODUCTION

Weak gravitational lensing is the most powerful tool for measuring the clustering of dark matter at low redshifts. Cosmic shear analyses use the correlated ellipticities of lensed galaxies to infer the power spectrum of foreground mass fluctuations. In galaxy–galaxy lensing, one correlates a shear map with the distribution of foreground galaxies to infer the galaxy-matter cross-correlation. This cross-correlation probes the halo mass profiles and dark matter environments of different classes of galaxies (e.g. Mandelbaum

et al. 2006), a valuable diagnostic of galaxy formation physics. The cross-correlations can be combined with measurements of galaxy clustering to infer the amplitude of matter clustering and thereby test dark energy or modified gravity theories for the origin of cosmic acceleration (Weinberg et al. 2013).

The opportunity is easy to understand at the level of linear perturbation theory, which should describe matter clustering and galaxy bias on large scales where clustering is weak. In this regime, the galaxy and matter autocorrelations are related by a scale-independent bias factor,  $\xi_{gg}(r) = b_g^2 \xi_{mm}(r)$ . The galaxy–galaxy lensing (hereafter GGL) signal is proportional to  $\Omega_m \xi_{gm}(r) = \Omega_m r_{gm} b_g \xi_{mm}(r)$ , where  $\Omega_m$  is the matter density parameter and the galaxy-matter cross-correlation coefficient  $r_{gm}$  is expected to

\* E-mail: [wibking.1@osu.edu](mailto:wibking.1@osu.edu)

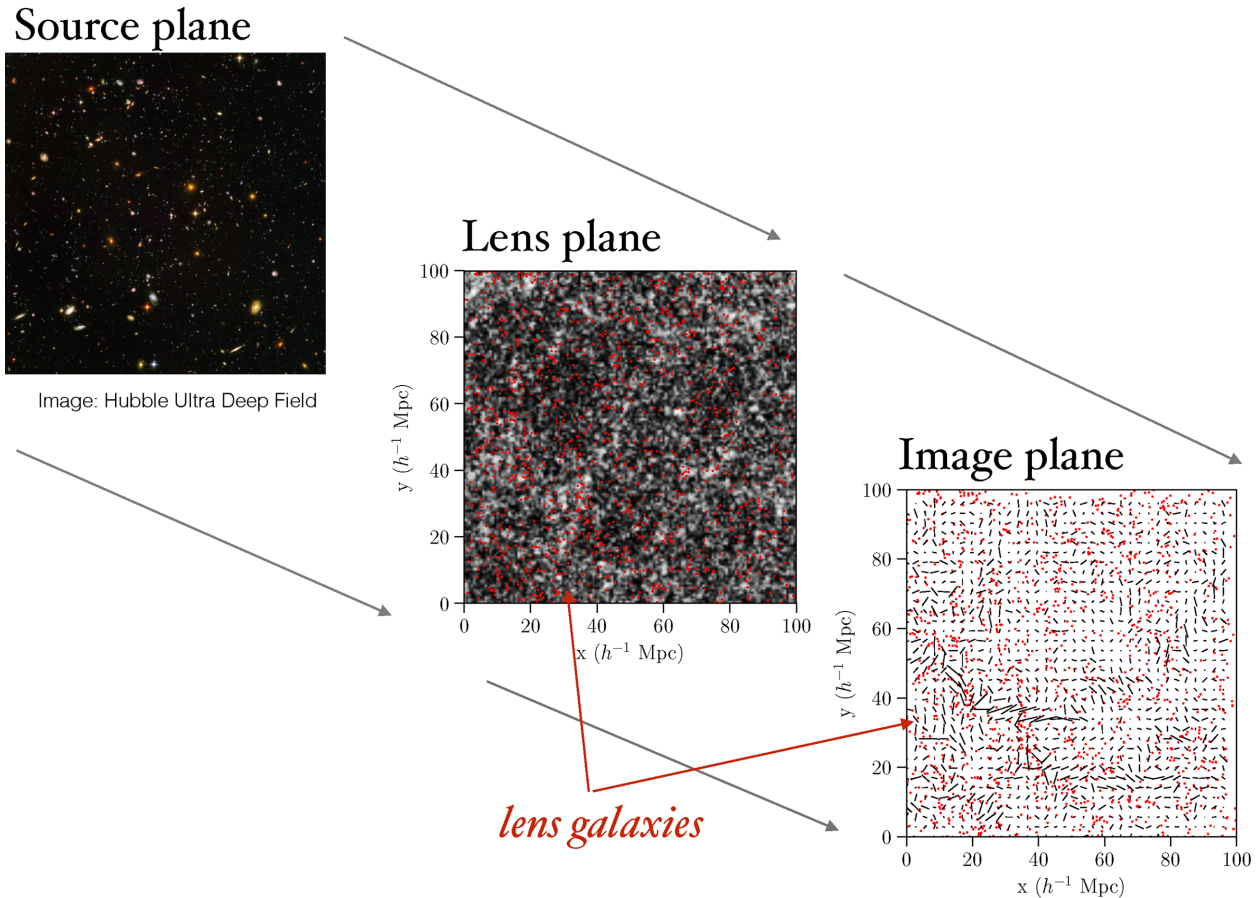


**Figure 1.** Pictorial illustration of clustering+GGL. The central panel shows the galaxy distribution (red points) and projected matter distribution (grey scale) in a  $400 h^{-1}$  Mpc slice through our fiducial simulation at  $z = 0.3$ . More distant source galaxies (illustrated here by the Hubble Ultra Deep Field) are sheared by the intervening dark matter. The cross-correlation of the galaxy distribution and the shear field (shown by lines in the right-hand panel, with arbitrary normalization) is the GGL signal, which can be combined with the galaxy clustering to infer the dark matter clustering at the redshift of the lens population.

approach one on large scales. Assuming  $r_{\text{gm}} = 1$ , one can combine the GGL and  $\xi_{\text{gg}}(r)$  measurements to cancel the unknown bias factor  $b_g$  and constrain  $\Omega_m \sqrt{\xi_{\text{mm}}(r)}$ . The amplitude of this observable can be summarized by the product  $\sigma_8 \Omega_m$ , where  $\sigma_8$  is the rms linear theory matter fluctuation in  $8 h^{-1}$  Mpc spheres. In practice, the best-constrained parameter combination differs from  $\sigma_8 \Omega_m$  because the value of  $\Omega_m$  affects the shape of the matter correlation function and because geometric distance factors that enter the lensing signal depend on  $\Omega_m$  (see discussion in Jain & Seljak 1997 and in Section 2.5 below). We illustrate the GGL measurement pictorially in Fig. 1. In this paper, we use cosmological  $N$ -body simulations and halo occupation distribution (HOD; Berlind & Weinberg 2002) methods to predict galaxy clustering and GGL into the deeply non-linear regime, where  $b_g$  may become scale-dependent and  $r_{\text{gm}}$  may depart from unity. We illustrate the considerable gains that can be made by exploiting small-scale GGL and  $\xi_{\text{gg}}$  measurements in these analyses.

Several previous studies have investigated the use of HODs or related methods to model GGL and galaxy clustering into the non-linear regime (Yoo et al. 2006; Cacciato et al. 2009; Leauthaud et al. 2011; Cacciato et al. 2012; Yoo & Seljak 2012; Cacciato et al. 2013; More et al. 2013; More 2013) and sharpen the resulting cosmological constraints. These studies have generally relied on analytic approximations with some numerical simulation tests, but

the precision of observations has reached the point that the accuracy of the analytic approximations is becoming a limiting factor. Our approach is similar in spirit to the numerically based ‘emulator’ scheme introduced by Heitmann et al. (2009) to predict non-linear matter power spectra. More recently, an emulator approach was used for a cosmological analysis of cluster lensing by Murata et al. (2018). We adopt a similar approach here, combining simulations with HOD models to predict  $\xi_{\text{gm}}$  and  $\xi_{\text{gg}}$ . We ultimately plan to consider a grid of cosmological parameters that spans the space allowed by cosmic microwave background (CMB) data, but in this paper we consider a fiducial cosmology based on *Planck* CMB results (Planck Collaboration et al. 2016) plus four simulations with fixed steps in  $\sigma_8$  and  $\Omega_m$  (at fixed  $\Omega_m h^2$ ). For our fiducial HOD, we consider parameters appropriate to the LOWZ sample of the Baryon Oscillation Spectroscopic Survey (BOSS; Eisenstein et al. 2011; Dawson et al. 2013), as the combination of imaging from the Sloan Digital Sky Survey (SDSS; York et al. 2000) with BOSS LOWZ spectroscopy is one of the most powerful current data sets for clustering and GGL analysis (Singh et al. 2017). Instead of the Gaussian Process emulator of Heitmann et al. (2009), we use a simple linear Taylor expansion in cosmological and HOD parameters. This approach becomes viable when the observational constraints about fiducial parameters are tight, but its adequacy must be tested in the context of any specified data analysis.

HOD methods characterize the relation between galaxies and dark matter in terms of the probability  $P(N|M_{\text{halo}})$  that a halo of mass  $M_{\text{halo}}$  contains  $N$  galaxies of a specified class (Benson et al. 2000). The principal question for cosmological inference from GGL and clustering is whether the adopted HOD parametrization has enough freedom to represent non-linear galaxy bias at the level of accuracy required in order to model the observations. The clustering of dark matter haloes depends on their formation history as well as their mass, an effect commonly known as halo assembly bias (Sheth & Tormen 2004; Gao, Springel & White 2005; Harker et al. 2006; Wechsler et al. 2006). Correlations of galaxy properties with halo assembly history at fixed mass can therefore induce galaxy assembly bias, which is not accounted for in traditional HOD parametrizations. Analysing the mock galaxy catalogues of Hearin & Watson (2013) and McEwen & Weinberg (2016) show that even when the model galaxy population has substantial assembly bias, fitting it with a standard HOD yields a cross-correlation coefficient  $r_{\text{gm}}(r)$  accurate at the  $\sim 2$  per cent level and thus predicts the correct relative amplitude of galaxy clustering and GGL. In this paper, we explicitly allow for variation of the HOD with large-scale environment in our parametrization, as a way of accounting for galaxy assembly bias (see Section 2.4).

GGL measurements can be made with the same imaging data sets acquired for cosmic shear analyses, though there are advantages to combining deep imaging data with a spectroscopic survey of galaxies that serve as the lensing sample. Mandelbaum et al. (2013) analysed galaxy clustering and GGL in the SDSS DR7 (Abazajian et al. 2009) data set, restricting their analysis to large scales where one can expect  $r_{\text{gm}} = 1$ . They found  $\sigma_8(\Omega_m/0.25)^{0.57} = 0.80 \pm 0.05$ , which can be scaled to the now commonly used parameter  $S_8 = \sigma_8(\Omega_m/0.3)^{0.5} = 0.72 \pm 0.05$  (where we ignore the small difference between 0.5 and 0.57 in the exponent). This is lower than the value  $S_8 = 0.83 \pm 0.012$  inferred for a  $\Lambda$  cold dark matter ( $\Lambda$ CDM) model normalized to the *Planck* 2015 CMB data (Planck Collaboration et al. 2016, Table 4, TT+TE+EE+lowP+lensing column).

Many but not all recent cosmic shear analyses also find low amplitudes for matter clustering compared to *Planck* value (e.g. Heymans et al. 2012; Hildebrandt et al. 2017; but see Jee et al. 2016). More et al. (2015) use an analytic HOD-based approach to model clustering of the BOSS CMASS galaxy sample (effective redshift  $z = 0.57$ ) and GGL measurements of CMASS from the  $105 \text{ deg}^2$  of overlap between BOSS and the Canada-France-Hawaii Telescope Lensing Survey (Heymans et al. 2012). Their results are consistent with *Planck*-normalized  $\Lambda$ CDM predictions, but the errors are fairly large because of the limited overlap area. Most recently, the Dark Energy Survey (DES) Collaboration has derived  $S_8 = 0.783_{-0.025}^{+0.021}$  from the combination of clustering, GGL, and cosmic shear in their Year 1 data set, weakening but not eliminating the tension with *Planck*  $\Lambda$ CDM predictions (DES Collaboration et al. 2017, table II).

Particularly relevant to this paper, Leauthaud et al. (2017) find discrepancies of 20–40 per cent, well above their statistical errors, at scales  $r < 10 h^{-1} \text{ Mpc}$  between their measurements of GGL for CMASS galaxies (from CFHTLenS and SDSS Stripe 82 imaging) and the numerical predictions from *Planck*-normalized mock catalogues that reproduce observed CMASS galaxy clustering. They conclude that the discrepancy might be a result of complex galaxy formation physics, and other effects such as incompleteness of the galaxy sample or miscentring of galaxies in haloes could play a role (see More et al. 2015). The stakes for robust modelling of non-linear galaxy clustering and GGL are therefore high, and the prospects for high-precision measurements over a range of redshifts will grow

rapidly with future DES analyses and forthcoming data from the Subaru Hyper-Suprime Camera (Aihara et al. 2018).

The next section describes the construction of our emulator, including the simulation suite, our HOD prescription and formulation of assembly bias, and the sensitivity of clustering and GGL observables to parameter variations about our fiducial choices. In Section 3, we derive forecasts for constraints on  $\sigma_8$ ,  $\Omega_m$ , and HOD parameters, using covariance matrices appropriate to BOSS LOWZ galaxy clustering and SDSS-depth GGL measurements (Singh et al. 2017). We show how the expected constraints depend on the choice of scales in the galaxy clustering and GGL measurements and on the effective source density of the weak-lensing map. In Section 4, we discuss the implications of our results and the prospects for applying our methodology to current and near-future data sets.

## 2 EMULATOR CONSTRUCTION

Our goal is to provide numerically calibrated analytic recipes to compute the real-space matter auto-correlation  $\xi_{\text{mm}}(r)$ , galaxy autocorrelation  $\xi_{\text{gg}}(r)$ , and galaxy-matter cross-correlation  $\xi_{\text{gm}}(r)$  for cosmological parameters and HOD parameters that are perturbations around a fiducial model. From these, one can compute projected observables that are directly measurable in a galaxy redshift survey or weak-lensing survey (see Section 2.5 below). Our fiducial cosmological parameters, based on the *Planck* 2015 CMB analysis (Planck Collaboration et al. 2016) are  $\Omega_m = 0.3142$ ,  $\Omega_b = 0.0491$ ,  $h = 0.6726$ ,  $n_s = 0.9652$ , and a linear theory power spectrum normalization at  $z = 0$  of  $\sigma_8 = 0.83$ . We assume a flat universe with a cosmological constant and three massless neutrino species ( $N_{\text{eff}} = 3.04$ ) with zero cosmological neutrino density. In this paper, we consider variations of  $\sigma_8$  and  $\Omega_m$ , the two parameters that most affect the relative amplitude of galaxy clustering and GGL. When varying  $\Omega_m$  we hold  $\Omega_m h^2$ ,  $\Omega_b h^2$ ,  $n_s$ , and  $\sigma_8$  fixed.

For fiducial HOD parameters, we choose values appropriate to the BOSS LOWZ galaxy sample at median redshift  $z = 0.27$  (see Section 2.3). Our methods can be readily extended to other galaxy samples and other redshifts chosen on the basis of specified observational data sets.

### 2.1 Numerical simulations

Our simulation procedures are described in detail by Garrison et al. (2017). They use the ABACUS  $N$ -body code (Ferrer et al., in preparation; Metchnik & Pinto, in preparation; see also Metchnik 2009) and initial conditions computed with the configuration-space 2LPT code described by Garrison et al. (2016). The input power spectra were generated by the linear Boltzmann code CAMB (Lewis & Challinor 2011) for redshift  $z = 0$  and rescaled by the linear growth factor to the starting redshift  $z = 49$ .

For the results in this paper, we use the simulations that consist of a fiducial cosmology favoured by the *Planck* 2015 results, two variations in  $\Omega_m$  (0.2879, 0.3442) at fixed  $\Omega_m h^2$ , and two variations in  $\sigma_8$  (0.78, 0.88). All of these simulations use the same phases in their initial conditions in order to minimize cosmic variance in the computation of derivatives (see Section 2.5). These simulations have a box size of  $720 h^{-1} \text{ Mpc}$ , a particle mass of  $1.09 \times 10^{10} h^{-1} M_\odot$  (for the fiducial  $\Omega_m$ ), with  $1440^3$  particles, and a Plummer softening length of  $41 h^{-1} \text{ kpc}$ . We use the particle outputs at redshift  $z = 0.3$  in this work, close to the central redshift of BOSS LOWZ (Parejko et al. 2013; Tojeiro et al. 2014). We refer to distances and densities in comoving units throughout this paper.



## 2.2 Halo identification

We identify haloes using the ROCKSTAR halo finder (Behroozi, Wechsler & Wu 2013). However, we use strict (i.e. without unbinding) spherical overdensity (SO) halo masses around the halo centres identified with ROCKSTAR, rather than the default 6D Friends-of-Friends-like masses output by ROCKSTAR. For finding haloes, we use a primary mass definition set to the virial mass of Bryan & Norman (1998), but for all halo masses used after halo finding is complete we adopt the  $M_{200b}$  mass definition, i.e. the mass enclosed by an SO of 200 times the mean matter density at a given redshift and cosmology. (Isolated haloes identified under the virial halo mass definition are not reclassified as subhaloes, even though a small fraction of them would not be isolated if the halo finder were rerun with the 200b halo definition.) Thus, although ROCKSTAR is our identification tool, our eventual halo population consists of dark matter systems with masses and radii defined by the  $200\rho_b$  criterion, effectively centred on local peaks of the dark matter density. We do not make use of dark matter subhaloes contained within larger haloes, although subhalo masses are always included in parent halo masses.

We have found that the reported concentration parameters ( $c = R_{\text{halo}}/R_s$  for an NFW profile; Navarro, Frenk & White 1997) are not reliable at the mass and force resolution available in our simulations. To obtain concentrations for creating satellite galaxy distributions, therefore, we use the fitting formula of Correa et al. (2015)

$$\log c = \alpha + \beta \log M_{\text{halo}} [1 + \gamma (\log M_{\text{halo}})^2], \quad (1)$$

with parameters  $\alpha(z)$ ,  $\beta(z)$ , and  $\gamma(z)$  functions of redshift that are calibrated to significantly higher resolution simulations. We rescale from the halo masses defined by 200 times the critical density ( $M_{200c}$ ) used there to the  $M_{200b}$  definition employed in this work, multiplying the  $200c$  concentration by  $\sqrt{2}$  to obtain an approximate value for the  $200b$  concentration (Hu & Kravtsov 2003).

## 2.3 HOD prescription

Our HOD model is similar to that introduced by Zheng et al. (2005) and used in many galaxy clustering analyses (e.g. Zehavi et al. 2005, Zehavi et al. 2011; Coupon et al. 2012; Zu & Mandelbaum 2015). Each halo of a given mass can host central galaxies and satellite galaxies.

To remove fluctuations in individual stochastic realizations of the HOD, we employ a weighting scheme similar to that of Zheng & Guo (2016), effectively averaging over many HOD realizations. We compute the expectation value that a given halo will host a central galaxy according to:

$$\langle N_{\text{cen}} | M_{\text{halo}} \rangle = \frac{1}{2} \left[ 1 + \operatorname{erf} \left( \frac{\log M_{\text{halo}} - \log M_{\text{min}}}{\sigma_{\log M}} \right) \right], \quad (2)$$

where  $M_{\text{min}}$  is the halo mass for which the occupation probability is one-half, and  $\sigma_{\log M}$  allows for logarithmic scatter between galaxy luminosity and halo mass. Throughout this paper, we use log for the base-10 logarithm and ln to indicate the natural logarithm. The central galaxy is placed at the ROCKSTAR-identified halo centre, with a weight set according to its expectation value. We compute the expectation value of the number of satellite galaxies according to:

$$\langle N_{\text{sat}} | M_{\text{halo}} \rangle = \begin{cases} \langle N_{\text{cen}} | M_{\text{halo}} \rangle \left( \frac{M_{\text{halo}} - M_0}{M_1} \right)^\alpha & \text{if } M_{\text{halo}} > M_0 \\ 0 & \text{otherwise.} \end{cases} \quad (3)$$

Here,  $M_0$  is a halo mass below which there are no satellite galaxies,  $M_1 + M_0$  is the halo mass for which there is an average of one satellite galaxy, and  $\alpha$  is the power-law slope of the number of satellites as a function of halo mass. Satellite galaxy counts in a given halo are assumed to be described by a Poisson distribution with this expectation value, so we weight each point in a cloud of  $N_{\text{cloud}}$  satellite galaxy sampling points in a given halo according to the ratio  $\langle N_{\text{sat}} | M_{\text{halo}} \rangle / N_{\text{cloud}}$ . We choose  $N_{\text{cloud}}$  to be at least 10 times the expectation value for a given halo (with a minimum of five sampling points per halo for haloes with a non-zero satellite number expectation value). The positions of satellite galaxy sampling points are chosen by sampling from a satellite galaxy profile:

$$\rho_{\text{sat}}(r) = r^{\Delta\gamma} \rho_{\text{NFW}}(r), \quad (4)$$

where  $\rho_{\text{NFW}}(r)$  is the NFW density profile with concentration computed from the fitting formula of Correa et al. (2015) and the parameter  $\Delta\gamma$  allows a power-law deviation between the satellite galaxy profile and the NFW profile of the mass distribution. [The quantity  $\Delta\gamma$  is unrelated to the  $\gamma$  of equation (1).] We truncate the satellite density profile at the  $R_{200,b}$  radius. Our weighting scheme based on halo centres and satellite galaxy sampling points is similar to that of Zheng & Guo (2016), but here we compute all quantities (i.e. correlation functions and number densities) using weights from each halo, rather than computing tables of weights in bins of halo mass.<sup>1</sup>

In an HOD analysis, the number density of galaxies is an important constraint in addition to the galaxy clustering. For our emulator and forecasts, we have elected to take  $n_{\text{gal}}$  as an HOD parameter in place of  $M_{\text{min}}$ . Once other parameters have been specified, we use equations (2) and (3) to find the value of  $M_{\text{min}}$  that yields the specified  $n_{\text{gal}}$ , keeping the ratios  $M_0/M_{\text{min}}$  and  $M_1/M_{\text{min}}$  fixed. The value of  $M_0/M_{\text{min}}$  is often ill constrained in HOD fits because it has negligible impact on number density or clustering for  $M_0/M_1 \ll 1$ . In this paper, we have chosen to fix  $M_0/M_1 = 0.089$  and not treat it as a free parameter; our results would be negligibly different if we set  $M_0 = 0$ , and almost unchanged if we marginalized over  $M_0/M_1$  (see Tables 1 and 2 below). Our set of adjustable HOD parameters is therefore  $n_{\text{gal}}$ ,  $\sigma_{\log M}$ ,  $M_1/M_{\text{min}}$ ,  $\alpha$ , and  $\Delta\gamma$ . For our fiducial model we adopt the values  $n_{\text{gal}} = 3 \times 10^{-4} h^3 \text{Mpc}^{-3}$ ,  $\sigma_{\log M} = 0.68$ ,  $M_1/M_{\text{min}} = 9.55$ ,  $\alpha = 1.15$ , and  $\Delta\gamma = 0$  with the number density based on the LOWZ results of Parejko et al. (2013) and the other parameter values based on the  $M_r < -21$  results of Zehavi et al. (2011). We choose the non-number density parameter values from another sample because they are significantly better constrained for the  $M_r < -21$  sample but still consistent with the values inferred by modelling by Parejko et al. (2013) of the LOWZ sample itself.

## 2.4 Modelling galaxy assembly bias

Part of the motivation for HOD descriptions of galaxy bias (see e.g. Berlind & Weinberg 2002) was the expectation from the simplest formulations of excursion set theory (Bond et al. 1991) that halo clustering should be independent of halo formation history at fixed halo mass (White 1994). While this prediction proved a good match to early  $N$ -body results (Lemson & Kauffmann 1999), more detailed

<sup>1</sup>Accumulating pair weights in double precision is critical to obtaining correlation functions that are not dominated by floating point round-off error.

**Table 1.** Forecasts of fractional uncertainties in cosmological and HOD parameters for various scenarios. For some scenarios, we show the forecast where the S/N is rescaled to match the S/N of the fiducial forecast (indicated by ‘rescaled S/N’).

	$\Delta \ln n_{\text{gal}}$	$\Delta \ln \sigma_{\log M}$	$\Delta \ln \frac{M_1}{M_{\min}}$	$\Delta \ln \alpha$	$\Delta Q_{\text{env}}$	$\Delta \gamma$	$\Delta \ln \Omega_m$	$\Delta \ln \sigma_8$
Fiducial	0.050	0.105	0.241	0.164	0.029	0.408	0.071	0.047
10x source density	0.049	0.067	0.194	0.148	0.018	0.343	0.049	0.032
Excluding $\gamma_t < 5 h^{-1}$ Mpc	0.050	0.236	0.379	0.171	0.061	0.423	0.080	0.060
Excluding $\gamma_t < 5 h^{-1}$ Mpc (rescaled S/N)	0.050	0.218	0.357	0.167	0.053	0.420	0.076	0.057
Excluding $w_p < 5 h^{-1}$ Mpc	0.050	0.419	0.762	1.288	0.092	2.546	0.105	0.101
Excluding $w_p < 5 h^{-1}$ Mpc (rescaled S/N)	0.050	0.233	0.496	1.001	0.046	1.279	0.045	0.057
Excluding both $< 5 h^{-1}$ Mpc	0.050	1.694	4.866	5.282	0.120	33.739	0.137	0.125
Excluding $< 2 (\gamma_t)$ and $< 4 (w_p) h^{-1}$ Mpc	0.050	0.693	2.145	3.087	0.087	4.932	0.095	0.088
Excluding $< 12 (\gamma_t)$ and $< 8 (w_p) h^{-1}$ Mpc	0.050	2.053	5.855	6.146	0.362	45.710	0.162	0.178
$\Delta \ln n_{\text{gal}} = 0.01$	0.010	0.096	0.234	0.163	0.029	0.408	0.071	0.047
$\Delta \ln n_{\text{gal}} = 0.1$	0.097	0.127	0.262	0.165	0.029	0.409	0.071	0.047
No lensing	0.050	0.257	0.452	0.234	0.067	0.454	0.120	0.110
$r_{\min} = 0.1 h^{-1}$ Mpc	0.048	0.061	0.089	0.107	0.020	0.056	0.058	0.040
Centrals only	0.043	0.020	—	—	0.023	—	0.070	0.044
Including $M_0/M_1$ as a free parameter	0.050	0.115	0.430	0.234	0.031	0.570	0.072	0.049
Marginalizing over concentration–mass relation	0.050	0.107	0.247	0.302	0.030	2.218	0.072	0.047

**Table 2.** Best-constrained parameters for forecasts.

	$p$	Best-constrained $\sigma_8 \Omega_m^p$
Fiducial	0.605	0.019
10x source density	0.618	0.009
Excluding $\gamma_t < 5 h^{-1}$ Mpc	0.690	0.023
Excluding $\gamma_t < 5 h^{-1}$ Mpc (rescaled S/N)	0.726	0.015
Excluding $w_p < 5 h^{-1}$ Mpc	0.882	0.040
Excluding $w_p < 5 h^{-1}$ Mpc (rescaled S/N)	0.988	0.036
Excluding both $< 5 h^{-1}$ Mpc	0.845	0.049
Excluding $< 2 (\gamma_t)$ and $< 4 (w_p) h^{-1}$ Mpc	0.828	0.041
Excluding $< 12 (\gamma_t)$ and $< 8 (w_p) h^{-1}$ Mpc	0.990	0.077
$\Delta \ln n_{\text{gal}} = 0.01$	0.605	0.018
$\Delta \ln n_{\text{gal}} = 0.1$	0.605	0.019
No lensing	-0.255	0.105
$r_{\min} = 0.1 h^{-1}$ Mpc	0.658	0.014
Centrals only	0.589	0.014
Including $M_0/M_1$ as a free parameter	0.622	0.020
Marginalizing over concentration–mass relation	0.603	0.019

measurements with larger simulations have revealed a variety of correlations between formation history and halo clustering (e.g. Sheth & Tormen 2004; Gao et al. 2005; Harker et al. 2006; Wechsler et al. 2006; Salcedo et al. 2018). These correlations can cause the galaxy HOD to vary systematically with halo environment, in which case a calculation that assumes a single global HOD will make incorrect predictions for galaxy clustering and GGL. For example, a model in which galaxy stellar mass is tied to halo peak circular velocity (rather than halo mass) and galaxy colour is tied to halo formation time exhibits significant ‘galaxy assembly bias’ for samples defined by luminosity and colour cuts; correlation functions change significantly if galaxies are shuffled among haloes of the same mass in a way that erases correlations with halo assembly (Zentner, Hearin & van den Bosch 2014).

To allow for assembly bias effects in our HOD model, we have introduced a parameter  $Q_{\text{env}}$  that shifts the cut-off  $M_{\min}$  of the

central galaxy occupation as a function of the halo’s large-scale environment. Specifically, we compute the overdensity  $\delta_8$  around each halo in a top-hat sphere of radius  $8 h^{-1}$  Mpc and rank all haloes (from 0 to 1) in order of increasing  $\delta_8$  in narrow (0.1 dex) bins of halo mass. We then choose an environment-dependent  $M_{\min}$  for each halo according to

$$\log M_{\min} = \log M_{\min,0} + Q_{\text{env}} [\text{rank}(\delta_8) - 0.5], \quad (5)$$

with a halo at the median overdensity for its mass having  $M_{\min} = M_{\min,0}$ . This prescription is similar to that introduced by McEwen & Weinberg (2016), but using halo rank instead of  $\delta_8$  directly makes the result for a given  $Q_{\text{env}}$  less dependent on the specific choice of environmental variable. It is also fairly intuitive, e.g. for  $Q_{\text{env}} = 0.1$  the haloes at the environmental extremes have  $M_{\min}$  across a range of 0.1 dex about that of haloes in the median environment. Although we fix  $M_1/M_{\min}$  in the case where  $Q_{\text{env}} = 0$ , we decouple

the satellite occupation from the central occupation when there is assembly bias, such that the satellite occupation does not change when  $Q_{\text{env}}$  is non-zero. Since the satellite occupation is unaffected, one-halo scales are essentially unaffected by  $Q_{\text{env}}$ . As we note in Section 3.2, the purpose of this parameter is to decouple the large-scale bias from that inferred from the small-scale clustering and lensing, rather than to provide a specific physical model of assembly bias. Although constructed based on the environmental overdensity rather than the concentration parameter of a halo, our parameter has effects on the correlation functions similar to that of the  $\mathcal{A}_{\text{cen}}$  parameter considered in Hearin et al. (2016) and used in a clustering analysis of SDSS galaxies by Zentner et al. (2016).

## 2.5 Emulated quantities

We use CORRFUNC (Sinha & Garrison 2017) to compute the real-space galaxy autocorrelation  $\xi_{\text{gg}}$ , galaxy-matter cross-correlation  $\xi_{\text{gm}}$ , and matter autocorrelation  $\xi_{\text{mm}}$  on scales  $0.01 < r < 110 h^{-1}$  Mpc. Separately, we compute the linear matter autocorrelation  $\xi_{\text{mm, lin}}$  by computing the appropriate integral over the linear power spectrum used for the initial conditions.

Our emulator uses finite differences to compute a linear Taylor expansion for ratios of these quantities as a function of scale:

$$b_{\text{nl}} = \left[ \frac{\xi_{\text{mm}}}{\xi_{\text{mm, lin}}} \right]^{1/2}, \quad (6)$$

$$b_{\text{g}} = \left[ \frac{\xi_{\text{gg}}}{\xi_{\text{mm}}} \right]^{1/2}, \quad (7)$$

$$r_{\text{gm}} = \left[ \frac{\xi_{\text{gm}}^2}{\xi_{\text{gg}} \xi_{\text{mm}}} \right]^{1/2}. \quad (8)$$

We focus on ratios so that the influence of cosmological parameters is treated exactly in the linear regime; there is no need to use a numerical emulator to approximate the impact of parameter changes on the linear matter power spectrum (similar to the methodology of Mandelbaum et al. 2013, who used a linear Taylor expansion in  $b_{\text{nl}}^2$  in order to model the non-linear matter correlation function). We expect this approach to give our emulator a wide range of validity, as the scale-dependence of non-linear corrections, galaxy bias, and  $r_{\text{gm}}(r)$  should have a relatively weak dependence on parameters such as  $\Omega_b$ ,  $h$ , and  $n_s$ . We will test this expectation using our larger simulation grid in future work.

Our emulation formula is simply:

$$X(r) = X_{\text{fid}}(r) + \sum_i \Delta p_i \frac{\partial X(r)}{\partial p_i} \quad (9)$$

where  $X(r)$  may be  $\ln b_{\text{nl}}(r)$ ,  $\ln b_{\text{g}}(r)$ , or  $\ln r_{\text{gm}}(r)$ ,  $X_{\text{fid}}(r)$  is the value in the fiducial model,  $\Delta p_i = p_i - p_{i, \text{fid}}$  is the difference in parameter  $i$  between the emulated model and the fiducial model, and the derivatives are evaluated about the fiducial model. The specific parameters that we use are:  $\ln \sigma_8$ ,  $\ln \Omega_m$ ,  $\ln n_{\text{gal}}$ ,  $\ln \sigma_{\log M}$ ,  $\ln M_1/M_{\text{min}}$ ,  $\ln \alpha$ ,  $\Delta \gamma$ , and  $Q_{\text{env}}$ . We generally expect logarithmic derivatives to give a greater range of validity because they can represent power-law relations not just linear relations, but we use linear derivatives for  $\Delta \gamma$  and  $Q_{\text{env}}$  because their fiducial values are zero.

We compute the partial derivatives in equation (9) by centred finite differences with step sizes determined by our set of grid points in cosmological and HOD parameter space. The HOD parameter space used consists of individual parameter variations

about the fiducial HOD (evaluated at the fiducial cosmology) at  $n_{\text{gal}} = \{0.00027, 0.00033\}$ ,  $\sigma_{\log M} = \{0.58, 0.78\}$ ,  $M_1/M_{\text{min}} = \{9.05, 10.05\}$ ,  $\alpha = \{1.0, 1.3\}$ ,  $\Delta \gamma = \{-0.1, 0.1\}$ , and  $Q_{\text{env}} = \{-0.1, 0.1\}$ . In Appendix B, we tabulate our values of  $\xi_{\text{mm, lin}}(r)$ ,  $b_{\text{nl, fid}}$ ,  $b_{\text{g, fid}}$ ,  $r_{\text{gm, fid}}$ , and the partial derivatives, allowing anyone to reproduce our emulator predictions.

The direct observables that we wish to emulate are the projected galaxy correlation function  $w_p(r_p)$  and the excess surface density  $\Delta \Sigma(r_p)$ . Neglecting sky curvature, residual redshift-space distortion, and higher order lensing corrections, these are related to the 3D real-space correlation functions by the projection integrals

$$w_p(r_p) = 2 \int_0^{\pi_{\text{max}}} \xi_{\text{gg}} \left( \sqrt{r^2 + \pi^2} \right) d\pi, \quad (10)$$

$$\Delta \Sigma(r_p) = \bar{\rho} \left[ \frac{4}{r_p^2} \int_0^{r_p} r \int_0^{\infty} \xi_{\text{gm}} \left( \sqrt{r^2 + \pi^2} \right) d\pi dr - 2 \int_0^{\infty} \xi_{\text{gm}} \left( \sqrt{r_p^2 + \pi^2} \right) d\pi \right], \quad (11)$$

where the cosmic mean matter density is given in comoving coordinates

$$\bar{\rho} = \Omega_m \left( \frac{3H_0^2}{8\pi G} \right). \quad (12)$$

We report  $w_p$  and  $\Delta \Sigma$  in units of  $h^{-1}$  Mpc and  $h M_{\odot} \text{pc}^{-2}$ , respectively.

We compute the 3D correlation functions from our emulator via

$$\xi_{\text{gg}} = b_{\text{g}}^2 \left( b_{\text{nl}}^2 \xi_{\text{mm, lin}} \right), \quad (13)$$

$$\xi_{\text{gm}} = r_{\text{gm}} b_{\text{g}} \left( b_{\text{nl}}^2 \xi_{\text{mm, lin}} \right), \quad (14)$$

where all quantities in both equations depend on the 3D separation  $r$ .

The choice of the  $\pi_{\text{max}}$  cut-off for computing  $w_p(r_p)$  depends on the redshift survey analysis; ideally one would like  $\pi_{\text{max}} \rightarrow \infty$  to eliminate redshift-space distortions entirely, but estimates of  $w_p(r_p)$  can become noisy for very large  $\pi_{\text{max}}$ . In this paper, we choose  $\pi_{\text{max}} = 100 h^{-1}$  Mpc. We assume that the impact of residual redshift-space distortion is accounted for in the redshift survey analysis. On the largest scales we consider, the redshift-space correction to  $w_p$  may be as large as 15 per cent for our chosen value of  $\pi_{\text{max}}$  (van den Bosch et al. 2013).

The computation of  $\Delta \Sigma$  from GGL observations depends on photometric redshift estimates for the source galaxies and on cosmological parameters used to compute lensing critical surface densities (e.g. Mandelbaum et al. 2005). In a cosmological analysis, one might instead use our emulator to predict the more directly observed mean tangential shear

$$\gamma_t(\theta) = \int dz_{\text{lens}} \int dz_{\text{src}} n_{\text{lens}}(z_{\text{lens}}) n_{\text{src}}(z_{\text{src}}) \Theta(z_{\text{src}} - z_{\text{lens}}) \times \frac{\Delta \Sigma(\theta, z_{\text{lens}})}{\Sigma_c(z_{\text{lens}}, z_{\text{src}})}, \quad (15)$$

where the step function  $\Theta(x)$  ensures that lensing contributions occur only when  $z_{\text{lens}} < z_{\text{src}}$ . equation (15) can incorporate the cosmological dependence of distance ratios, nuisance parameters for photometric redshift uncertainties, and any signal-to-noise (S/N) weighting applied to the observations (through additional factors

modifying  $\Delta\Sigma$ ). The (comoving) critical surface density  $\Sigma_c$  is

$$\Sigma_c = \frac{c^2}{4\pi G} \frac{D_C(z_{\text{src}})}{D_C(z_{\text{lens}})[D_C(z_{\text{src}}) - D_C(z_{\text{lens}})](1 + z_{\text{lens}})}, \quad (16)$$

where  $D_C(z)$  denotes the comoving distance to redshift  $z$ .

For the purpose of the forecasts in this paper, we compute  $\gamma_t(r_p)$  predictions from our emulator assuming that  $n_{\text{lens}}$  is a delta function centred at the effective lens redshift  $z_{\text{lens}} = 0.27$  (computed for BOSS LOWZ by Singh et al. 2017) and  $n_{\text{src}}$  is a  $\delta$ -function centred at an effective source redshift  $z_{\text{src}} = 0.447$ , chosen so that the resulting critical lensing surface density is equal to the value  $\Sigma_c = 4.7 \times 10^3 h M_\odot \text{pc}^{-2}$  given by Singh et al. (2017). Using  $\gamma_t$  instead of  $\Delta\Sigma$  as the observable in our forecasts introduces an additional dependence on cosmology that significantly modifies the  $\Omega_m$ – $\sigma_8$  degeneracy direction, as the distances entering  $\Sigma_c$  involve an integral over the factor  $[\Omega_m(1+z)^3 + \Omega_\Lambda]^{-1/2}$ . We find  $\text{dln } \Sigma_c(z_{\text{lens}}, z_{\text{src}}; \Omega_m)/\text{dln } \Omega_m \approx 0.12$  at our fiducial values of  $\Omega_m$ ,  $z_{\text{lens}}$ , and  $z_{\text{src}}$ . Since  $\gamma_t \propto \Delta\Sigma \Sigma_c^{-1}$ , this dependence modifies the best-constrained cosmological parameter by a factor  $\approx \Omega_m^{-0.12}$ . Because the amplitude of the lensing signal  $\gamma_t$  has an additional dependence on  $\Omega_m$  beyond that of  $\Delta\Sigma$ , using  $\gamma_t$  marginally improves the constraining power of the measurement compared to assuming that  $\Delta\Sigma$  is the observable.

Additionally, we correct for the  $\Omega_m$ -dependence of the projected distance as a function of angular separation and redshift  $r_p(\theta, z; \Omega_m)$  by assuming the observer has estimated projected distances in an  $\Omega_m = 0.3$  universe. We thus rescale the ‘true’ distances in which we measure our correlation functions to those our observer would compute when calculating  $w_p$  and  $\Delta\Sigma$  (equations 10 and 11). However, we find that this correction is very small and makes almost no difference to our results.

### 3 FORECASTING CONSTRAINTS

#### 3.1 Covariance matrices

We use the following expressions from Singh et al. (2017) for the Gaussian component of the observable covariances:

$$\text{cov}_{w_p}(r_i, r_j) = \frac{2A_{ij}}{A_i A_j} \int_0^\infty \frac{k dk}{2\pi} J_0(kr_i) J_0(kr_j) \left( b_g^2 P(k) + \frac{1}{n_g} \right)^2, \quad (17)$$

$$\begin{aligned} \text{cov}_{\Delta\Sigma}(r_i, r_j) &= \frac{V_{ij}}{V_i V_j} \int_0^\infty \frac{k dk}{2\pi} J_2(kr_i) J_2(kr_j) \\ &\times \left[ \left( b_g^2 P(k) + \frac{1}{n_g} \right) \left( \Delta\Pi \bar{\rho}^2 P(k) + \frac{\Sigma_c^2 \sigma_\gamma^2}{n_s} \right) \right. \\ &\left. + \Delta\Pi (\bar{\rho} b_g r_{\text{gm}} P(k))^2 \right]. \quad (18) \end{aligned}$$

These expressions neglect line-of-sight modes, terms that can arise from using a suboptimal estimator that does not subtract the tangential shear around random points, and redshift evolution over the lensed galaxy population. We convert the  $\Delta\Sigma$  covariance to our lensing observable  $\gamma_t$  covariance by

$$\text{cov}_{\gamma_t}(r_i, r_j) = \text{cov}_{\Delta\Sigma}(r_i, r_j) \Sigma_c^{-2}. \quad (19)$$

The area and volume normalization factors in these expressions are:

$$A_{ij} = \int_0^\infty \frac{k dk}{2\pi} J_0(kr_i) J_0(kr_j) [W(k)]^2, \quad (20)$$

$$A_i = \int_0^\infty \frac{k dk}{2\pi} J_0(kr_i) [W(k)]^2, \quad (21)$$

$$V_{ij} = L_W A_{ij}, \quad (22)$$

$$V_i = L_W A_i. \quad (23)$$

Following Singh et al. (2017), we adopt survey parameters appropriate to BOSS LOWZ GGL. The window function corresponds to a circular survey on the sky of radius  $R_s = 1275 h^{-1} \text{Mpc}$ ,

$$W(k) = 2\pi R_s^2 \frac{J_1(kR_s)}{kR_s}, \quad (24)$$

where  $n_g = 3 \times 10^{-4} h^3 \text{Mpc}^{-3}$  is the galaxy number density,  $\Delta\Pi = 400 h^{-1} \text{Mpc}$  is the effective line-of-sight lensing distance,  $L_W = 500 h^{-1} \text{Mpc}$  is the effective line-of-sight survey window,  $\Sigma_c = 4.7 \times 10^3 h M_\odot \text{pc}^{-2}$  is the critical lensing surface density,  $\sigma_\gamma = 0.21$  is the shape noise per galaxy,  $n_s = 8 h^2 \text{Mpc}^{-2}$  is the effective projected number density of source galaxies,  $\bar{\rho} = \Omega_m (3H_0^2/8\pi G)$  is the cosmic mean matter density (in comoving coordinates), and  $P(k)$  is the non-linear matter power spectrum as computed from our fiducial simulation. At our adopted lens redshift, the survey area is  $9000 \text{deg}^2$  and the nominal source density is  $1 \text{arcmin}^{-2}$ . This nominal value is reduced to an effective source density of  $0.3 \text{arcmin}^{-2}$  due to redshift cuts (contributing a  $\sim 50$  per cent reduction) and by S/N weighting (contributing a  $\sim 30$  per cent reduction) (Singh, personal communication).

The correlation matrices

$$\text{corr}(r_i, r_j) = \frac{\text{cov}(r_i, r_j)}{\sqrt{\text{cov}(r_i, r_i) \text{cov}(r_j, r_j)}} \quad (25)$$

for our fiducial forecast are shown in Fig. 2. The  $\gamma_t$  correlation matrix is nearly diagonal because of the dominant contribution from shot noise, while the  $w_p$  correlation matrix has substantial off-diagonal terms for  $r_p > 2 h^{-1} \text{Mpc}$ . For purposes of the forecast, we assume that non-Gaussian contributions to the covariance (e.g. Scoccimarro, Zaldarriaga & Hui 1999; Cooray & Hu 2001) will be minimized by masking the largest several clusters from the survey in the clustering and GGL measurements used for cosmological analysis. We also assume that the cross-observable covariance (i.e. the covariance between  $\gamma_t$  and  $w_p$ ) is negligible and the contribution to the covariance from uncertainties in our knowledge of the true cosmic mean observables due to the finite size of our simulations is negligible, although we plan to quantify these contributions to the covariance in future work.<sup>2</sup>

#### 3.2 Model predictions

Fig. 3 shows the predicted  $w_p(r)$  and  $\gamma_t(r)$  from applying our fiducial HOD to our fiducial cosmological simulation (black curve) and to the simulations with higher  $\sigma_8$  (blue dashed) and higher  $\Omega_m$  (green dot-dashed). On the scale of this figure, the impact of these parameter changes (6 per cent in  $\sigma_8$  and 10 per cent in  $\Omega_m$ ) is barely discernible, but one can see that the fractional changes to  $\gamma_t(r)$  are larger than the fractional changes to  $w_p(r)$ . Increasing  $\sigma_8$  boosts

<sup>2</sup>The covariance between clustering and GGL has been derived for angular separations (Marian, Smith & Angulo 2015), but not, as far as we are aware, in the case of a projected correlation function  $w_p(r_p)$ .



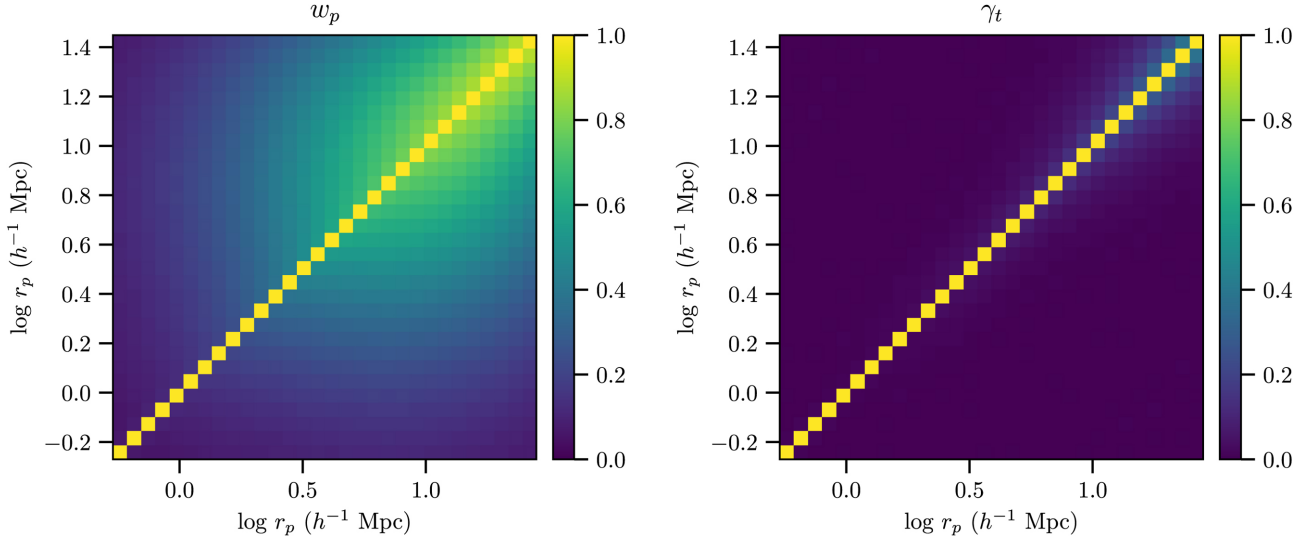


**Figure 2.** The correlation matrices for our forecast. We compute the covariance matrix for  $\gamma_t$  with the integrals for the Gaussian contributions to the covariance for the variance-minimizing estimator described by Singh et al. (2017). We use similar integrals to compute the covariance for clustering. We assume a source density, area, and redshift properties similar to those of the BOSS LOWZ spectroscopic sample for clustering measurements and SDSS imaging for lensing source galaxies.

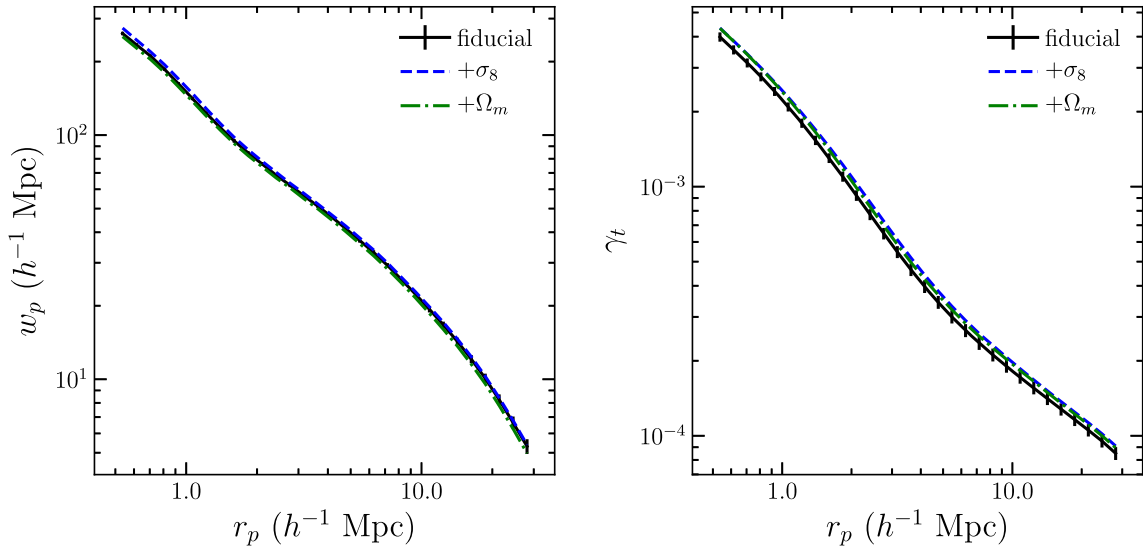


**Figure 3.** Projected correlation function (left) and tangential shear (right) predicted for our fiducial HOD parameters and the fiducial cosmological simulation (black solid) and for simulations with  $\sigma_8$  increased by 6 per cent (blue dashed) or  $\Omega_m$  increased by 10 per cent (green dot-dashed). Error bars on the black curve show the diagonal errors for our assumed data properties, corresponding to BOSS LOWZ lens galaxies and SDSS-depth imaging. The magnitude of changes can be seen more clearly in Figs 4 and 5.

$\xi_{\text{mm}}(r)$ , but at fixed number density  $n_{\text{gal}}$  the galaxy bias  $b_g$  decreases. For  $w_p \propto b_g^2 \xi_{\text{mm}}$  the effects nearly cancel, while for  $\gamma_t \propto b_g \xi_{\text{mm}}$  there is a net increase of amplitude. Increasing  $\Omega_m$  changes the shape of  $\xi_{\text{mm}}(r)$  and thus of  $w_p(r)$ , but the effect of a 10 per cent change is subtle. Increasing  $\Omega_m$  boosts the amplitude of  $\gamma_t(r)$  mainly by increasing the  $\bar{\rho}$  pre-factor of  $\Delta\Sigma$  in equation (11); the change to  $\Sigma_c$  in equation (15) goes in the opposite direction but with much smaller amplitude. The changes of observables are large compared to the statistical errors expected for our fiducial data assumptions, but we have not yet considered degeneracy between cosmological and HOD parameters.

Fig. 4 shows derivatives of  $\ln w_p(r)$  (left-hand panel) and  $\ln \gamma_t(r)$  (right-hand panel) with respect to our eight model parameters. The

top panels show derivatives for the conventional HOD parameters:  $\ln n_{\text{gal}}$ ,  $\ln \sigma_{\log M}$ ,  $\ln M_1/M_{\text{min}}$ ,  $\ln \alpha$ , and  $\Delta\gamma$ . For  $w_p(r)$ , the large-scale behaviour is constant in  $r_p$ , corresponding to changes in the asymptotic value of  $b_g$ , but the derivatives change below  $r_p \approx 2 h^{-1}$  Mpc as the one-halo contributions to  $\xi_{\text{gg}}(r)$  become important. Thus, the parameters have degenerate effects on linear scales, but using the full range of  $w_p(r)$  can break these degeneracies. Increasing  $n_{\text{gal}}$  decreases  $w_p(r_p)$  on all scales by shifting central galaxies to less-massive, more numerous, less-biased haloes. Increasing  $\sigma_{\log M}$  has a similar effect at large scales, and it suppresses  $w_p(r_p)$  more severely in the one-halo regime because more central galaxies reside in haloes that are not massive enough to host satellites. Increasing  $M_1/M_{\text{min}}$  decreases the overall fraction of satellites, depressing the



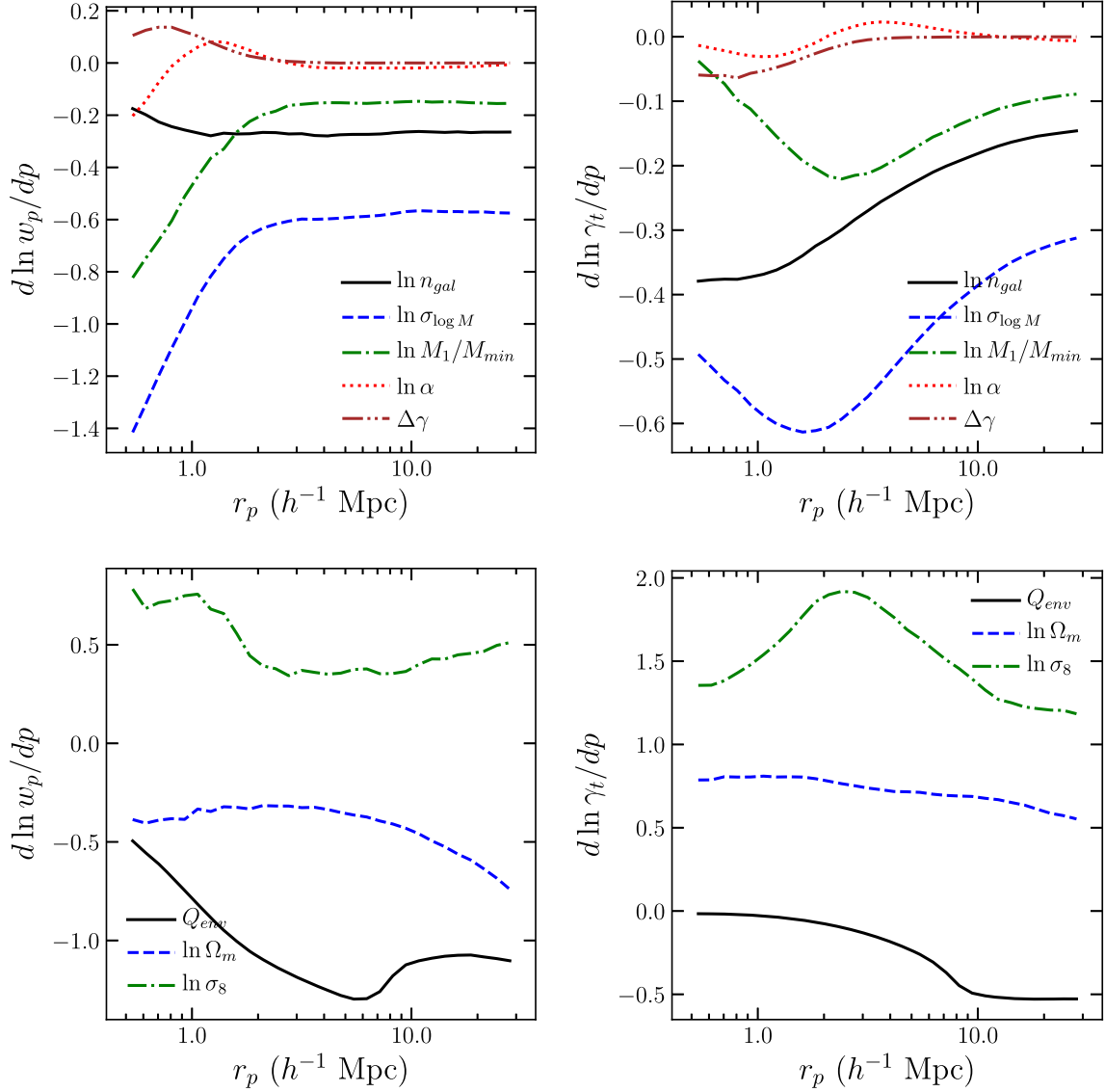


**Figure 4.** Logarithmic derivatives of  $w_p$  (left-hand panels) and  $\gamma_t$  (right-hand panels) with respect to HOD parameters and cosmological parameters, as indicated in the legends. Top panels show derivatives for standard HOD parameters. Bottom panels show derivatives for  $\sigma_8$ ,  $\Omega_m$ , and the environmental HOD parameter  $Q_{\text{env}}$ .

large-scale bias slightly and the one-halo correlations more severely. Increasing  $\alpha$  at fixed  $M_1/M_{\text{min}}$  has almost no impact at large scales, but it slightly boosts  $w_p(r_p)$  on scales corresponding to the virial radii of cluster mass haloes, and it depresses  $w_p(r_p)$  on small scales where lower mass haloes dominate the one-halo regime. Increasing  $\Delta\gamma$  has no impact in the two-halo regime, and it slightly boosts  $w_p(r_p)$  inside  $1 h^{-1}$  Mpc by steepening satellite galaxy profiles.

The influence of these parameters on  $\gamma_t(r_p)$  is qualitatively similar, but the scale dependence is more complex because  $\Delta\Sigma$  is an *excess* surface density,  $\Delta\Sigma(r_p) = \bar{\Sigma}(< r_p) - \bar{\Sigma}(r_p)$ , where  $\bar{\Sigma}(< r_p)$  is averaged over all radii smaller than  $r_p$  (see e.g. Sheldon et al. 2004). Even at  $r_p = 30 h^{-1}$  Mpc, the impact of  $n_{\text{gal}}$ ,  $\sigma_{\log M}$ , and  $M_1/M_{\text{min}}$  has not reached the scale-independence expected asymptotically at large  $r_p$ .

The lower panels of Fig. 4 show derivatives with respect to the cosmological parameters  $\ln \sigma_8$  and  $\ln \Omega_m$  and our environment-dependent HOD parameter  $Q_{\text{env}}$ . Increasing  $Q_{\text{env}}$  reduces the large-scale galaxy bias with other HOD parameters held fixed, because it

increases  $M_{\text{min}}$  (and thus decreases galaxy numbers) for haloes of a given mass in denser environments. The effect of  $Q_{\text{env}}$  becomes mildly scale-dependent inside the radius  $r = 8 h^{-1}$  Mpc that we use to define halo environment, and it decreases towards small scales because the one-halo regime of  $\xi_{\text{gg}}(r)$  or  $\xi_{\text{gm}}(r)$  depends only on integrals over the halo mass function and galaxy density profile (see Berlind & Weinberg 2002, equation 11). For our purposes, the most important effect of  $Q_{\text{env}}$  is that it decouples the large-scale bias from the conventional HOD parameters, so one cannot simply use small- and intermediate-scale constraints on these parameters to predict the large-scale  $b_g$  for a given cosmology.

Increasing  $\sigma_8$  boosts both  $w_p$  and  $\gamma_t$ , but the impact on  $w_p$  is smaller because of the cancellation with decreased galaxy bias at fixed  $n_{\text{gal}}$ . Raising  $\sigma_8$  shifts the inflection of  $\xi_{\text{mm}}(r)$  at the one- to two-halo transition outwards, because the virial radii of  $M_*$  haloes are slightly larger, which causes the jump in  $d \ln w_p / d \ln \sigma_8$  at the transition scale  $r_p \approx 1 - 2 h^{-1}$  Mpc. The corresponding effect in  $\gamma_t(r_p)$  is a bump in the derivative at somewhat larger scales.

Increasing  $\Omega_m$  with fixed  $\Omega_m h^2$  makes the matter power spectrum bluer in observable,  $h^{-1}$  Mpc units, decreasing  $w_p$  at large scales for fixed  $\sigma_8$ .<sup>3</sup> With linear evolution and linear bias, there would be a compensating boost to  $w_p$  at small scales, but in our non-linear calculation  $w_p$  is suppressed at all  $r_p$ . By contrast, increasing  $\Omega_m$  boosts  $\gamma_t(r_p)$  because of the  $\bar{\rho}$  factor in equation (11), but the logarithmic derivative is below one because of the reduction in  $\xi_{\text{mm}}(r)$  and the increase of  $\Sigma_c$  in equation (15).

For a more concrete illustration of parameter impacts, Fig. 5 shows the fractional changes to  $\gamma_t(r_p)$  and  $w_p(r_p)$  that arise from changing  $M_1/M_{\text{min}}$  by  $\pm 0.50$  from the fiducial value of 9.55, changing  $Q_{\text{env}}$  by  $\pm 0.1$  from the fiducial value of 0.0, or changing  $\sigma_8$  by  $\pm 0.05$  from the fiducial value of 0.83. Here, we have computed  $\xi_{\text{gg}}(r)$  and  $\xi_{\text{gm}}(r)$  directly from the populated simulations, but because these correspond to the same finite-difference step sizes we use to compute the  $b_{\text{nl}}$ ,  $b_g$ , and  $r_{\text{gm}}$  derivatives, the results from using our emulator would be identical.

Changing  $M_1/M_{\text{min}}$  alters the large-scale amplitude of  $w_p(r_p)$  and  $\gamma_t(r_p)$ , and the impact grows at small scales in  $w_p(r_p)$  and intermediate scales in  $\gamma_t(r_p)$ . The effect of  $Q_{\text{env}}$ , by contrast, is largest at large scales, decreasing to nearly zero at sub-Mpc scales in  $\gamma_t$ . Raising or lowering  $\sigma_8$  raises or lowers the large scale  $w_p(r_p)$  and  $\gamma_t(r_p)$  as expected, and non-linear evolution induces a distinctive scale dependence on scales of a few  $h^{-1}$  Mpc and below. The fact that each parameter produces a different scale dependence and has different effects on the two observables demonstrates the potential of precise measurements across the full range of scales to break degeneracies between cosmological quantities and ‘nuisance’ parameters that describe the relation between galaxies and dark matter.

### 3.3 Information and Forecasts

Fig. 6 shows the parameter constraint forecasts for our fiducial scenario, which adopts the  $w_p$  and  $\gamma_t$  covariance matrices of Fig. 2 and a Gaussian prior on  $\ln n_{\text{gal}}$  with a width of 5 per cent. All of the forecast parameters are in terms of the natural logarithm of the usual parameter, except for parameters that may plausibly be zero or negative (i.e.  $Q_{\text{env}}$  and  $\Delta\gamma$ ). With analysis down to scales of  $0.5 h^{-1}$  Mpc, a data combination like BOSS LOWZ and SDSS imaging can already yield impressively tight constraints. The best-constrained combination of cosmological parameters is  $\sigma_8 \Omega_m^p$  with  $p = 0.61$ , the forecast uncertainty is 1.9 per cent after marginalizing over all HOD parameters. The fully marginalized constraints on  $\sigma_8$  and  $\Omega_m$  individually are 4.7 per cent and 7.1 per cent, respectively.

The observational uncertainty in  $n_{\text{gal}}$  will reflect both cosmic variance and systematic uncertainties in completeness and evolutionary corrections. Here, we are treating our galaxy sample as volume-limited and characterized by a single space density, but a full observational analysis might require a redshift-dependent  $\bar{n}(z)$ . For the individual luminosity-threshold samples of BOSS CMASS galaxies studied by Guo et al. (2014), jackknife error estimates imply  $n_{\text{gal}}$  uncertainties of about 6 per cent (Guo, private communication). We find that the forecast constraint on  $n_{\text{gal}}$  is equal to our adopted prior. Fortunately, varying the  $n_{\text{gal}}$  prior has negligible impact on the cosmological parameter uncertainties; sharpening the prior to 1 per cent or loosening it to 10 per cent does not change the uncertainties in  $\sigma_8$ ,  $\Omega_m$ , or  $\sigma_8 \Omega_m^p$  by more than 0.1 per cent.

Of other HOD parameters, the most poorly constrained is  $\Delta\gamma$ , because its largest effects are limited to scales below the smallest  $r_p$  we consider. For the same reason, uncertainties in  $\Delta\gamma$  have little impact on the uncertainties in cosmological or other HOD parameters. Uncertainties in  $\sigma_{\log M}$ ,  $M_1/M_{\text{min}}$ , and  $\alpha$  are 11 per cent, 24 per cent, and 16 per cent, respectively. Interestingly, the assembly bias parameter  $Q_{\text{env}}$  is quite tightly constrained, with a forecast uncertainty of 0.029 dex. Changing the  $n_{\text{gal}}$  prior to 10 per cent (1 per cent) moderately loosens (tightens) the constraints on  $\sigma_{\log M}$  and  $M_1/M_{\text{min}}$  but has negligible effect on other parameters.

Tables 1 and 2 compare forecasts for a variety of other scenarios, with Table 1 listing the marginalized constraints on  $\sigma_8$ ,  $\Omega_m$ , and individual HOD parameters and Table 2 listing the best-constrained parameter combination of the form  $\sigma_8 \Omega_m^p$ . We first consider the impact of increasing the effective weak-lensing source density by a factor of 10–3 galaxies arcmin<sup>-2</sup>, comparable to the source density in the DES instead of SDSS imaging. This change lowers the shape noise contribution to the  $\gamma_t$  covariance matrix (equation 18). The precision of  $\sigma_8 \Omega_m^p$  improves by a factor of two, to 0.9 per cent. The individual constraints on  $\sigma_8$  and  $\Omega_m$  improve by a factor  $\approx 1.5$ .

Returning to the fiducial source density of 1 arcmin<sup>-2</sup>, we next consider the impact of eliminating the  $\gamma_t$  measurements at  $r_p < 5 h^{-1}$  Mpc. The constraint on  $\sigma_8 \Omega_m^p$  degrades to 2.3 per cent; the value of  $p$  in the best-constrained combination depends on the data being considered, increasing slightly to  $p = 0.69$  in this case. Degradation can arise from the loss of aggregate statistical precision in the  $\gamma_t(r_p)$  measurement – with fewer points, the overall amplitude is less well determined and from the loss of leverage on parameter degeneracies for the reduced range of scales. To isolate the second effect, we rescale the  $\gamma_t(r_p)$  covariance matrix  $C_{ij}$  by a constant factor that restores the  $S/N = [D^T C^{-1} D]^{1/2}$  to its value in the fiducial forecast, where  $D$  is the data vector. With this rescaling, the constraint on  $\sigma_8 \Omega_m^p$  improves relative to the fiducial forecast, from 1.9 per cent to 1.5 per cent. Of course, one is not able to make this adjustment in a real observational situation; the weak-lensing error bars at large scales do not decrease because one chooses to ignore small scales in the modelling. However, this experiment shows that the ‘per unit’ information content of the large-scale  $\gamma_t(r_p)$  measurements is more significant than the small-scale measurements because they suffer less degeneracy with galaxy bias parameters. The error bars on some HOD parameters, particularly  $\sigma_{\log M}$ ,  $M_1/M_{\text{min}}$ , and  $Q_{\text{env}}$ , do get worse when eliminating small-scale  $\gamma_t(r_p)$  and rescaling the covariance matrix.

For  $w_p(r_p)$ , the situation is reversed. Excluding points with  $r_p < 5 h^{-1}$  Mpc degrades the precision on  $\sigma_8 \Omega_m^p$  by more than a factor of two, from 1.9 per cent to 4.0 per cent, and rescaling to restore the  $S/N$  of the fiducial measurement only improves the precision to 3.6 per cent. Without rescaling, the constraints on HOD parameters become dramatically worse, especially for the parameters  $\alpha$  and  $\Delta\gamma$  whose largest impact is on small scales. With rescaling, the constraints on all HOD parameters improve, but remain worse than the fiducial case (except for  $n_{\text{gal}}$ ), and the degeneracy with  $\sigma_8 \Omega_m^p$  is evidently large enough to degrade its precision. The marginalized error on  $\Omega_m$  itself improves by nearly a factor of 1.6 over the fiducial case because of the better measurement of the large-scale shape of  $w_p(r_p)$ , but the marginalized constraint on  $\sigma_8$  is moderately worse than the fiducial case. Overall, this experiment shows that the information from non-linear scales of  $w_p(r_p)$  improves the cosmological constraining power of clustering and GGL by breaking degeneracies with HOD parameters that describe the relation between galaxies and dark matter. We caution

<sup>3</sup>The power spectrum shape parameter  $\Gamma = \Omega_m h$  increases, shifting the turnover in  $P(k)$  to higher  $k$  in  $h$  Mpc<sup>-1</sup> units.

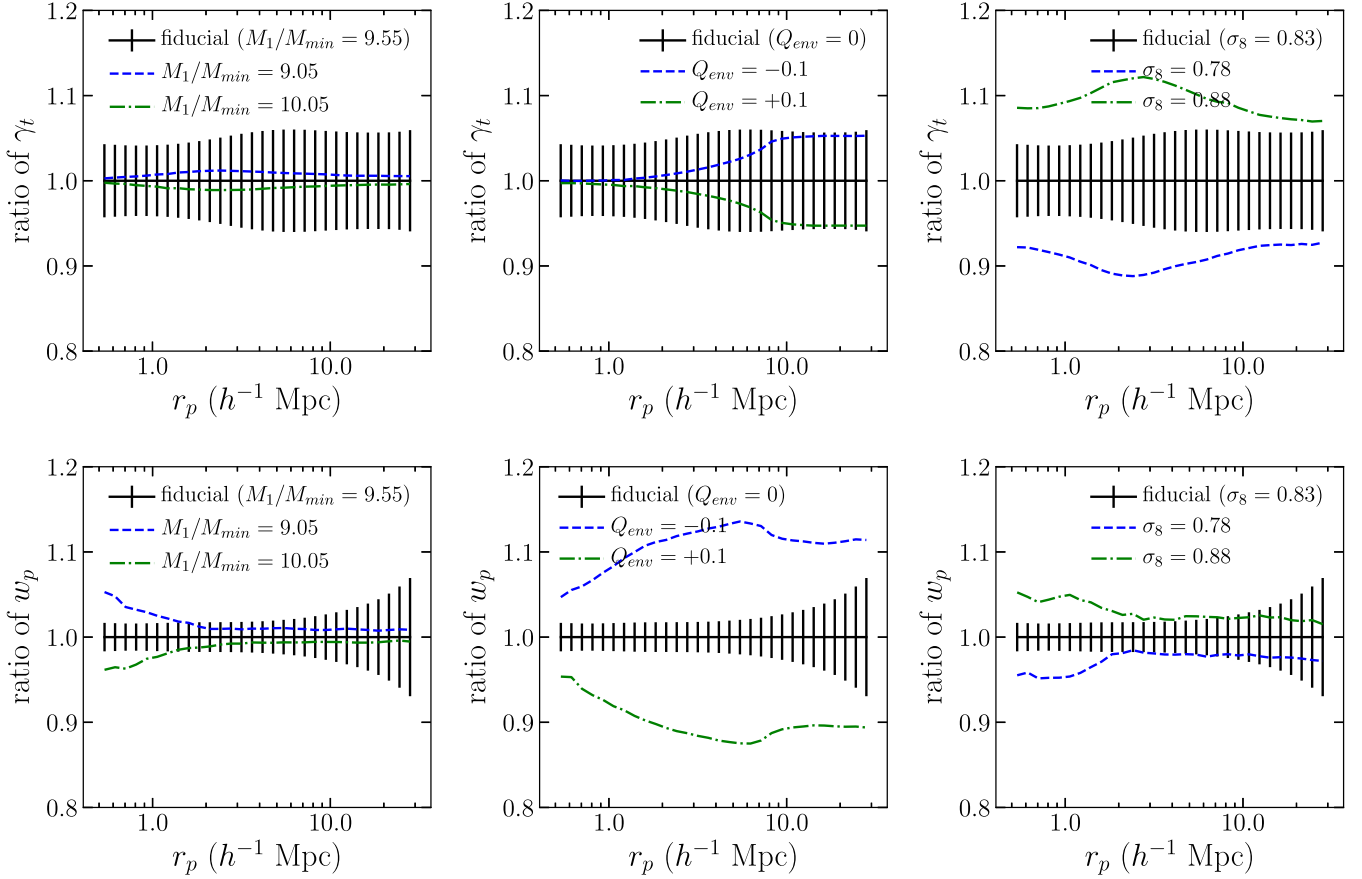


**Figure 5.** The ratios of observables for changes in some parameters. The leftmost panel shows the effect of the HOD parameter  $M_1/M_{min}$  on the observables  $w_p$  and  $\gamma_t$ . The middle panel shows the effect of the environmental density parameter  $Q_{env}$ , and the rightmost panel shows the effect of  $\sigma_8$ . The error bars are the same as those shown in Fig. 3.

that our Taylor expansion and Fisher matrix calculation may become inaccurate with large uncertainties in  $\alpha$  and  $\Delta\gamma$ , but this inaccuracy will not affect our qualitative conclusions.

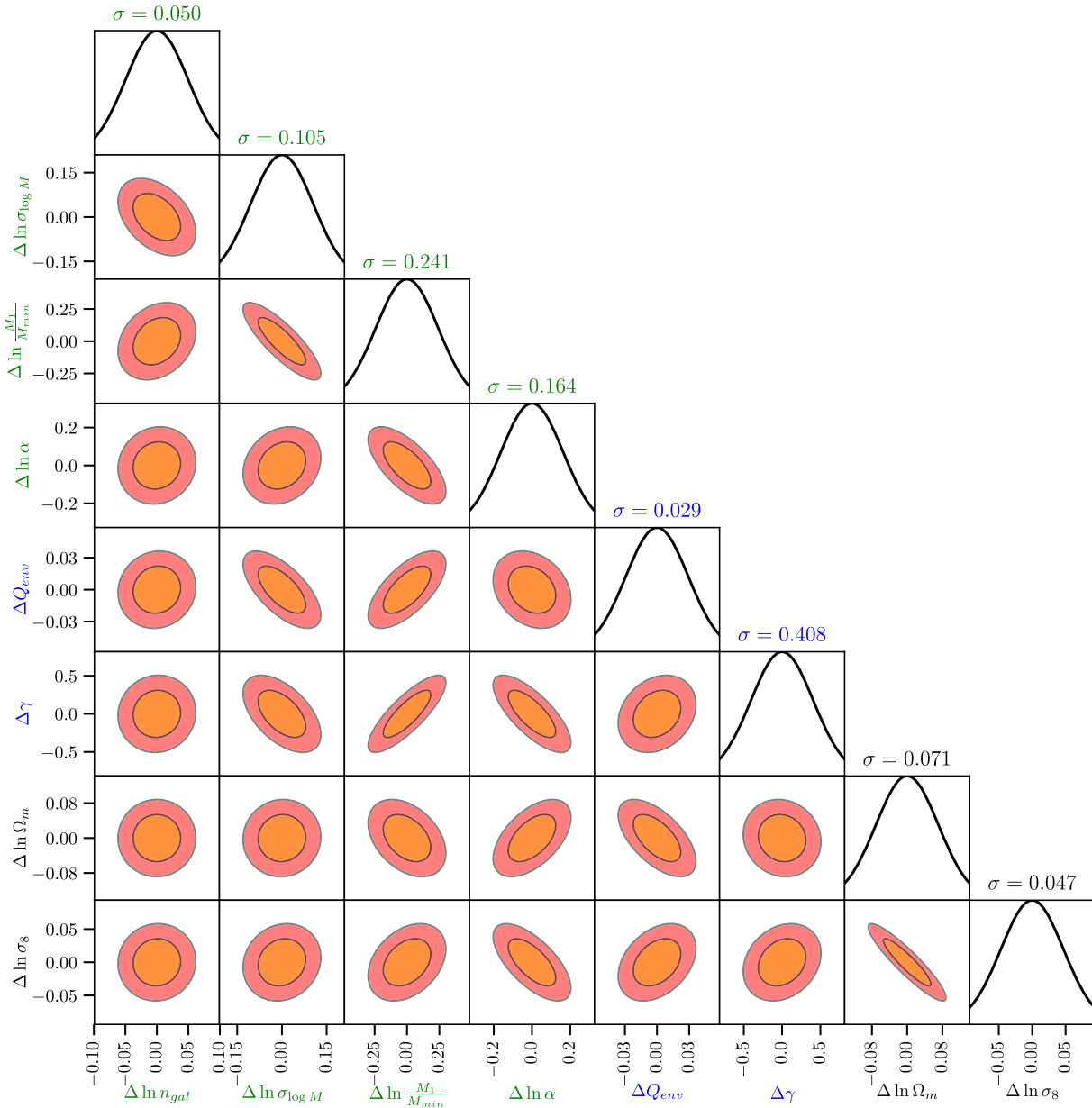
Finally, we consider the specific cuts adopted by Mandelbaum et al. (2013), excluding  $r_p < 2 h^{-1}$  Mpc for  $\gamma_t(r_p)$  and  $r_p < 4 h^{-1}$  Mpc for  $w_p(r_p)$ . These cuts increase the error on  $\sigma_8 \Omega_m^p$  by more than a factor of two, from 1.9 per cent to 4.1 per cent. The individual marginalized constraints on  $\sigma_8$  and  $\Omega_m$  grow by slightly less than a factor of two. We conclude that the gains in cosmological precision achievable from our more comprehensive theoretical modelling, relative to the more conservative approach of Mandelbaum et al. (2013), are about a factor of two in parameter errors, equivalent to the effect of a fourfold increase in survey area.

Fig. 7 provides further insight into the degeneracy of cosmological and HOD parameters and the role of  $w_p(r_p)$  and  $\gamma_t(r_p)$  in breaking them. The leftmost points on each sequence show the fractional uncertainty in  $\sigma_8$  if all HOD parameters and  $\Omega_m$  are held fixed to their true values. Our fiducial data combination could measure  $\sigma_8$  to 0.56 per cent if all other parameters were known perfectly. We then unleash the HOD parameters in sequence, adding successively more degrees of freedom to the HOD model. At each step in the sequence, we choose the parameter that produces the sharpest increase of the  $\sigma_8$  uncertainty when it is set free, for the fiducial data case. Ordered this way, the parameter with the highest leverage is  $n_{gal}$ , because with other HOD parameters fixed a 5 per cent uncertainty in  $n_{gal}$  (set by our prior) can change the galaxy bias

factor significantly. We previously found that varying the  $n_{gal}$  prior from 0.01 to 0.10 had negligible impact on cosmological precision (see Tables 1 and 2), but that was with other HOD parameters free to compensate for its effect. Adding more HOD parameters steadily increases the marginalized  $\sigma_8$  error, reaching 1.9 per cent with the full parameter set. Because of the usual cosmological degeneracy between  $\sigma_8$  and  $\Omega_m$ , the marginalized  $\sigma_8$  error rises to 4.7 per cent when  $\Omega_m$  is also free. However, the fractional error on  $\sigma_8$  with fixed  $\Omega_m$  is the same as the fractional error on the best-constrained  $\sigma_8 \Omega_m^p$  combination, and we view this as the best characterization of the statistical power of a combined clustering + GGL data set.

When small scales of  $\gamma_t(r_p)$  are dropped (green curve in Fig. 7), the precision on  $\sigma_8$  as the sole free parameter degrades by a factor of 1.5, from 0.56 per cent to 0.86 per cent. However, the uncertainty associated with scale-dependent galaxy bias is reduced when the small scale  $\gamma_t(r_p)$  are not considered, so the degradation with all HOD parameters free is only a factor of 1.2 (2.3 per cent versus 1.9 per cent, as listed in Table 2).

Dropping the small-scale  $w_p(r_p)$  data instead (red curve) produces minimal degradation when HOD parameters are fixed, but now these parameters are poorly constrained and thus have a large impact once they are set free. In particular, the assembly bias parameter  $Q_{env}$  has a much larger uncertainty in this case (see Table 1) and has a more pronounced impact on cosmological parameter uncertainty. Raising the weak-lensing source density (blue curve) improves the  $\sigma_8$  precision at fixed HOD by a factor of 2.5 (0.22 per cent versus



**Figure 6.** The fiducial forecast. We use the predicted projected galaxy correlation  $w_p$  and the mean tangential shear  $\gamma_t$  on scales  $0.5 < r_p < 30 h^{-1}$  Mpc. Tight cosmological constraints are possible (4.7 per cent on  $\sigma_8$  and 7.1 per cent on  $\Omega_m$ ) even after marginalizing over assembly bias and HOD parameters.

0.56 per cent), nearly the full factor of  $10^{1/3} = 3.16$  that would be expected if weak-lensing shape noise were the only effect limiting the measurement precision. The relative impact of galaxy bias uncertainties is larger when the weak-lensing precision is higher, but not drastically so; when all HOD parameters are free, the  $\sigma_8$  precision is still a factor of two better than that of the fiducial case (0.9 per cent versus 1.9 per cent).

We compare the fiducial scenario with a minimum scale cut of  $r_{p,\min} = 0.5 h^{-1}$  Mpc to a forecast where all projected scales down to  $r_{p,\min} = 0.1 h^{-1}$  Mpc are used. With additional small-scale information, the cosmological constraint on  $\sigma_8 \Omega_m^p$  improves by a factor of 1.4, largely due to reduced degeneracy with HOD parameters describing satellite galaxies (including the satellite galaxy profile parameter  $\Delta\gamma$ ). We choose not to use this as our fiducial forecast scenario since this scale cut may require accurate

modelling of halo substructure, whereas our fiducial scale cut should be less sensitive to simulation accuracy, correlations between satellite galaxies and subhaloes, and the effects of baryons on the matter distribution.

The ‘no lensing’ forecasts of Tables 1 and 2 show forecasts based on the  $w_p(r_p)$  data alone, with no GGL information. In a pure linear theory calculation with galaxy bias  $b_g$  as a free parameter, the shape of  $w_p(r_p)$  would constrain  $\Omega_m$ , but there would be no constraint on  $\sigma_8$  because it would be fully degenerate with  $b_g$ . Our non-linear forecast with an HOD description of galaxy bias yields an 11 per cent constraint on  $\sigma_8 \Omega_m^p$  and a 11 per cent marginalized constraint on  $\sigma_8$ . These are much worse than the 1.9 per cent and 4.7 per cent fiducial forecasts, demonstrating that the great majority of the cosmological information is coming from the *combination* of clustering and GGL, not from the high precision



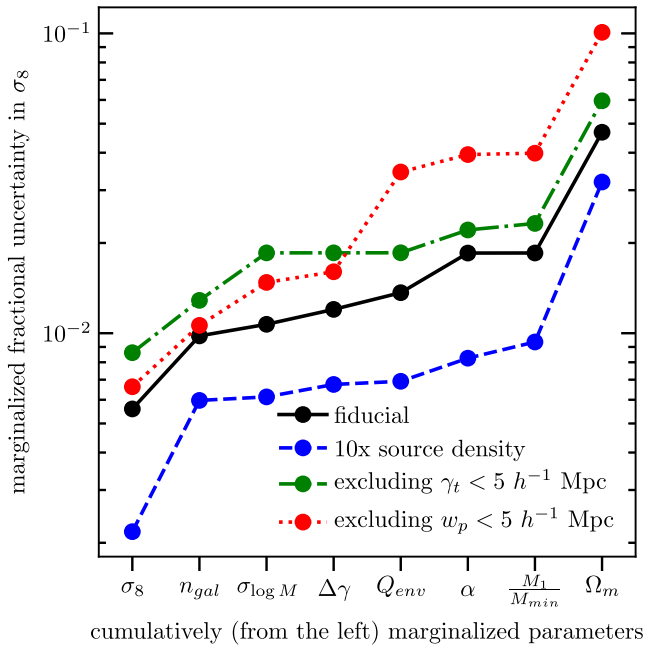


**Figure 7.** A comparison of forecasts on marginalized  $\sigma_8$  for various scenarios. We show the marginalized fractional uncertainty on  $\sigma_8$  as we marginalize over an increasing number of parameters from left to right. The order of parameters is set such that  $\Omega_m$  is chosen to be the last-marginalized parameter,  $\sigma_8$  is chosen to be the first parameter, and the other parameters are ordered such that the steepest rise in fractional uncertainty is obtained for the fiducial forecast scenario.

clustering measurements on their own. The uncertainty in  $Q_{\text{env}}$  is also substantially larger for the clustering only case (0.067 versus 0.029). This difference shows that, while some of the information about  $Q_{\text{env}}$  is coming from the distinctive scale dependence that it produces, much of it comes from the relative strength of clustering and GGL. This suggests that the clustering + GGL combination could be a useful diagnostic of galaxy assembly bias, especially if one has strong external constraints on  $\Omega_m$ . Physically, assembly bias is the main effect that can alter the large-scale galaxy bias given constraints on other HOD parameters from small and intermediate scales. The clustering + GGL combination breaks the degeneracy of  $b_g$  and  $\sigma_8$ , even on linear scales, so it can test for the presence or absence of this effect.

We include a forecast (‘centrals only’) for a hypothetical scenario in which we can correctly label all observed galaxies as central galaxies or satellite galaxies and then only use the central galaxies to compute the observed correlation functions and number densities. Some analytic forecasts (e.g. Yoo & Seljak 2012) and cosmological analyses of GGL implicitly assume all observed galaxies are centrals.

Using group catalogues, one could in principle try to identify a sample of central galaxies for clustering + GGL analyses. This strategy omits information (galaxy pairs and tangential shear involving satellites) but simplifies the model (no satellite HOD parameters), so the cosmological constraints could get better or worse. For our centrals-only forecast, we find that the constraint on the HOD parameter  $\sigma_{\log M}$  improves dramatically relative to our own fiducial forecast, from 0.105 to 0.020, because it is no longer degenerate with satellite HOD parameters. However, the constraints on  $\Omega_m$  and  $\sigma_8$  improve only slightly (from 0.071 to 0.070 and 0.047 to 0.044), and the  $\sigma_8 \Omega_m^p$  constraint tightens from 0.019 to

0.014. Thus, while including satellites does require additional HOD parameters, non-linear clustering provides sufficient information to constrain them so that the extra complexity does not degrade the cosmological results. The situation is very different if we exclude scales below  $8 h^{-1}$  Mpc; in this case, the centrals-only constraints are a factor of two better than constraints from the full galaxy population because large-scale clustering alone provides little leverage on the satellite population.

In practice, any identification of a centrals-only population will have systematic uncertainties of incompleteness and contamination. Given that our complete modelling with no central/satellite separation yields nearly the same cosmological constraining power, we advocate using all galaxies and modelling measurements into the non-linear regime.

We have carried out three additional tests in which we add a parameter to our fiducial forecast scenario. First we allow the central galaxy portion of the HOD to asymptote to a value  $f_{\text{cen}} < 1$ , to allow for the possibility that colour selection or other effects leave some high-mass haloes without a central galaxy in the sample. Marginalizing over  $f_{\text{cen}}$  does not degrade the cosmological constraints. An  $f_{\text{cen}} < 1$  also mimics the effects of halo miscentring – central galaxies that are offset from their halo potential minimum – so we conclude that this effect will also not degrade our cosmological constraints.<sup>4</sup> Second, we have checked that marginalizing over parameters of the concentration–mass relation used to determine the satellite galaxy profiles does not degrade the cosmological constraints. Instead, the concentration–mass parameters are highly degenerate with the  $\Delta\gamma$  parameter, implying that one can use either prescription to model uncertainty in the satellite galaxy profile but need not use both. Third, we have allowed  $M_0/M_1$  to be a free parameter [see equation (3)] instead of fixed at 0.089. Freeing the cut-off of the satellite HOD increases uncertainty in  $M_1/M_{\text{min}}$  and  $\alpha$ , but again the degradation of cosmological constraints is minimal.

One can also ask whether our first-order Taylor expansion emulator is sufficiently accurate for modelling a data combination like the ones considered here. As a preliminary test, we have drawn 20 samples from the posterior of the fiducial forecast while fixing cosmological parameters to those of the fiducial cosmology. Computing the galaxy populations and correlation functions numerically, we compare to the predictions of  $w_p$  from our emulator, finding that on scales greater than  $2 h^{-1}$  Mpc, the standard deviation of  $|w_{p,\text{num}} - w_{p,\text{emu}}|$  is substantially lower than the diagonal error bars derived from our covariance matrices. Within  $2 h^{-1}$  Mpc, however, we

<sup>4</sup>Strictly, this conclusion depends on the assumption that miscentring and central incompleteness have identical effects on the clustering and lensing signals, which will not be true if the miscentred centrals have an ensemble average spatial distribution within haloes differing from that of satellites or if the HOD of the combined miscentred central and satellite population cannot be represented in the nearly power-law form of equation (3). In our model, we always consider centrals to be the galaxy at the potential minimum of the halo and treat all other galaxies as satellites. There is no conclusive observational evidence that miscentred centrals need to be modelled distinctly from the normal satellite population, but the results of Ho et al. (2009) suggest that further investigation may be warranted. Generically, changes in the spatial distribution of centrals within their haloes only affect very small scales in the clustering signal but may alter the lensing signal on scales comparable to the one- to two-halo transition regimes. Since the degradation of cosmological constraints is minimal when we exclude lensing data on scales smaller than  $5 h^{-1}$  Mpc, it is reasonable to expect that additional parameters describing a spatially distinct central population may not significantly degrade the cosmological constraints.

find that the rms emulator error is comparable to the size of the diagonal error bars on our fiducial projected clustering signal. With respect to the lensing signal, we find that the emulator error is very subdominant compared to the error bars on  $\gamma_t$  on all scales that we use for forecasts. One route to improving emulator accuracy for  $w_p$  is to include second derivatives, or perhaps to adopt a different interpolation framework such as Gaussian processes (e.g. Heitmann et al. 2009). In modelling a specific galaxy sample, one would likely infer best-fitting HOD parameters, then retrain the emulator centring on this fiducial case. We leave the question of emulator accuracy with respect to cosmological parameters for a future paper using the full ABACUS cosmology grid (Garrison et al. 2017).

#### 4 DISCUSSION AND CONCLUSIONS

Several observational studies have demonstrated the promise of combining galaxy clustering and GGL to constrain cosmological parameters and test  $\Lambda$ CDM+GR predictions of matter clustering (Cacciato et al. 2009, 2013; Mandelbaum et al. 2013; More et al. 2015; Hildebrandt et al. 2017; Leauthaud et al. 2017; Prat et al. 2017; DES Collaboration et al. 2017). Building on earlier theoretical studies by Yoo et al. (2006), Leauthaud et al. (2011), Cacciato et al. (2012), and Yoo & Seljak (2012), our investigation demonstrates the power of extending these analyses down to small scales using a flexible model for the relation between galaxies and dark matter. As a fiducial case, we consider HOD parameters and covariance matrices scaled to the BOSS LOWZ galaxy lens sample and SDSS-depth imaging (approximately one source galaxy per arcmin<sup>2</sup>) over 9000 deg<sup>2</sup> (Singh et al. 2017) for weak-lensing measurements. Extending the analysis of  $\gamma_t(r_p)$  and  $w_p(r_p)$  to  $0.5 h^{-1}$  Mpc improves the precision of the best-constrained  $\sigma_8 \Omega_m^p$  combination by more than a factor of two (1.9 per cent versus 4.1 per cent) relative to the more conservative cuts ( $2 h^{-1}$  Mpc for  $\gamma_t$  and  $4 h^{-1}$  Mpc for  $w_p$ ) adopted by Mandelbaum et al. (2013) for their analysis of SDSS DR7, which uses the perturbative bias model of Baldauf et al. (2010). Some of the gain in parameter precision comes directly from using the small-scale  $\gamma_t(r_p)$  measurements, which provide additional leverage on the amplitude of the galaxy-matter cross-correlation. However, the largest gains come from using the smaller scales of  $w_p(r_p)$  to constrain HOD parameters, which allows our model to make better use of the large-scale  $\gamma_t(r_p)$  data for the cosmological constraints.

The emulator approach described in Section 2 makes a fully non-linear,  $N$ -body + HOD approach practical for statistical analysis. In this paper, we have considered only  $\sigma_8$  and  $\Omega_m$  as the varying cosmological parameters, and we have computed results at  $z = 0.3$ . However, because we construct our emulator to compute ratios of correlation functions starting from  $\xi_{\text{mm, lin}}$ , it may accommodate some range of cosmological parameters. We will improve the emulator in future work using a grid of cosmological simulations, which will also allow leave-one-out tests for the emulator's accuracy and more systematic study of its range of validity. Detailed predictions for an observational data set also require information about the redshift distributions of the lens and source samples and may include nuisance parameters that describe observational or theoretical systematics. Rather than incorporate these survey-specific elements into our emulator, we focus on predicting the two quantities,  $\xi_{\text{gg}}$  and  $\xi_{\text{gm}}$ , that require non-linear clustering calculations.

The main limitation of the emulator approach as pursued here is the need to retune the fiducial HOD for each galaxy lens sample, and to model the range of redshifts probed by that sample. This does not

require new simulations, but it does require new HOD populations and correlation function measurements for each lens sample being considered.

A novel aspect of our model is inclusion of a parametrized description of HOD environmental variation, to capture the potential effects of galaxy assembly bias. This prescription allows the large-scale galaxy bias to be at least partly decoupled from the ‘classic’ HOD parameters constrained by small- and intermediate-scale clustering. It is encouraging that this new degree of freedom in the galaxy bias model does not lead to substantial degradation of the cosmological parameter constraints. Indeed, we find that the combination of clustering and GGL gives interestingly tight constraints on  $Q_{\text{env}}$  even with free cosmological parameters. To date, most observational tests for galaxy assembly bias have focused on comparing clustering of blue and red galaxies, but the approach outlined here could provide a way to test for assembly bias in luminosity- or mass-selected galaxy samples. Our  $Q_{\text{env}}$  parametrization predicts a scale-dependence of galaxy bias that might be different from that predicted by a specific physical model that ties galaxy properties to halo assembly. The best way to test the adequacy of our model is to apply it to galaxy populations drawn from hydrodynamic simulations or to simulations that populate  $N$ -body haloes using abundance and age-matching prescriptions (e.g. Hearin & Watson 2013; Lehmann et al. 2017) or semi-analytic galaxy formation models. Hydrodynamic simulations are also needed to test for baryonic effects on the mass distribution, including the impact of subhaloes around satellite galaxies. Yoo et al. (2006) found little impact of subhaloes on GGL, but their hydrodynamic simulations were too small for tests at the level of precision needed for current data sets. More recently, GGL was considered by van Daalen et al. (2014) in the context of comparing hydrodynamic simulations with and without a given form of strong active galactic nucleus feedback. They found virtually no impact on GGL on scales larger than approximately twice the halo virial radius (when modelling galaxy samples as a function of number density rather than at fixed halo mass) but  $\sim 10$  per cent effects on smaller scales due to scale-dependent effects on  $\xi_{\text{gm}}$ , with substantially smaller effects on the scale-dependence of  $\xi_{\text{gg}}$ . Since the improved constraining power by using small scales in our forecasts is primarily due to the small-scale clustering rather than small-scale lensing, our results may be relatively insensitive to baryonic effects on the matter distribution, but more work is needed to assess any potential bias in cosmological parameters due to baryonic effects in our analysis framework.

The stakes for precise and accurate joint clustering and GGL analyses are high, because many cosmic shear and GGL analyses to date yield estimates of  $\sigma_8 \Omega_m^{0.5}$  that are lower than that predicted by a *Planck*-normalized  $\Lambda$ CDM model (e.g. Heymans et al. 2012; Hildebrandt et al. 2017; DES Collaboration et al. 2017). The statistical significance for any one data set is usually  $\lesssim 2\sigma$ . Improving lensing and CMB analyses could remove this tension, or they could sharpen it into strong evidence for new physics. The largest magnitude of discrepancy is found by Leauthaud et al. (2017), who measure GGL for BOSS CMASS galaxies from 250 deg<sup>2</sup> of deep imaging data and compare their measurements to predictions from a variety of mock catalogues that are designed to reproduce observed CMASS galaxy clustering. On scales of  $0.3 - 3 h^{-1}$  Mpc the discrepancy in  $\gamma_t(r_p)$  is about 20 per cent and well outside the statistical errors, and on scales of  $0.1 - 0.3 h^{-1}$  Mpc it is larger still. (However, we caution that the authors did not consider the possible effects of an incompleteness of the galaxy sample that is unexpectedly large or with a complicated halo mass dependence, or equivalently [under the assumptions

discussed in Section 3.3] miscentring of a large fraction [ $>0.2$ ] of central galaxies with respect to the halo centre, see e.g. More et al. 2015). The results of McEwen & Weinberg (2016) suggest that this discrepancy should be robust to uncertainties about galaxy assembly bias, because they find that even when strong assembly bias is present, an HOD model that reproduces the observed galaxy clustering also predicts the correct ratio  $\xi_{\text{gm}}(r)/\xi_{\text{gg}}(r)$ . Our results here provide further support for this view, showing that clustering and GGL can yield strong cosmological constraints even when marginalizing over our parametrized assembly bias prescription.

For our fiducial data assumptions, we forecast a 1.9 per cent error on  $\sigma_8\Omega_m^{0.61}$ . For comparison, the error on  $S_8 \equiv \sigma_8(\Omega_m/0.3)^{0.5}$  from DES Year 1 data is 2.9 per cent (DES Collaboration et al. 2017). This constraint uses clustering (Elvin-Poole et al. 2017) and GGL (Prat et al. 2017) of the DES ‘redMaGiC’ galaxy sample (Elvin-Poole et al. 2017; Rozo et al. 2016) and cosmic shear from the same imaging data (Troxel et al. 2017), comprising 26 million galaxy shape measurements over  $1321 \text{ deg}^2$  ( $5.4 \text{ gal arcmin}^{-2}$ ). The DES analysis includes marginalization over several systematics not considered here, such as shear calibration uncertainties, photometric redshift biases, and galaxy intrinsic alignments. These uncertainties must be accounted for in any GGL analysis, and they will degrade the precision of cosmological measurements below that of our forecasts. None the less, our results show that extending to non-linear scales allows even SDSS-depth imaging to achieve constraints competitive with the best current weak-lensing data sets.

Our emulator results (detailed in Appendix B) can be applied as they are to GGL measurements of the BOSS LOWZ sample (keeping in mind the caveats about emulator accuracy that we detail in Section 3.3). For imaging data significantly deeper than SDSS, better constraints will come from higher redshift lens populations that probe larger volumes, such as the BOSS CMASS spectroscopic sample or photometrically defined samples such as DES redMaGiC. We will investigate predictions for such samples in future work. There are many considerations that go into choosing a lens sample, including lens density and redshift distribution, overlap with deep imaging data for spectroscopic samples, accuracy of photometric redshifts for photometric samples, and observational uncertainties such as incompleteness, contamination, or depth variations. Our results suggest that physical simplicity should be an additional consideration in defining lens samples, since the extension of analyses to non-linear scales can substantially improve their constraining power but requires accurate modelling. Data sets emerging over the next few years should enable tests of the matter clustering predicted by General Relativity at the percent or even subpercent level, with the potential to reveal profound new physics or to provide powerful confirmation of the reigning theories of dark energy and cosmological gravity.

## ACKNOWLEDGEMENTS

We thank Chris Hirata, Eric Huff, Rachel Mandelbaum, Sukhdeep Singh, and Ying Zu for valuable conversations about this work.

BDW is supported by the National Science Foundation Graduate Research Fellowship Program under grant no. DGE-1343012. ANS is supported by the Department of Energy Computational Science Graduate Fellowship Program of the Office of Science and National Nuclear Security Administration in the Department of Energy under contract DE-FG02-97ER25308. BDW, ANS, and DHW are supported in part by National Science Foundation grant AST-1516997. LG and DJE have been supported by National Science Foundation grant AST-1313285. DJE is further supported by the

Department of Energy Office of Science grant DOE-SC0013718 and as a Simons Foundation Investigator. Any opinions, findings, and conclusions or recommendations expressed in this material are those of the author(s) and do not necessarily reflect the views of the National Science Foundation.

Simulations were analysed in part on computational resources of the Ohio Supercomputer Center (Center 1987), with resources supported in part by the Center for Cosmology and AstroParticle Physics at the Ohio State University. Some computations in this paper were performed on the El Gato supercomputer at the University of Arizona, supported by grant 1228509 from the National Science Foundation, and on the Odyssey cluster supported by the Faculty of Arts and Sciences Division of Science, Research Computing Group at Harvard University.

We gratefully acknowledge the use of the MATPLOTLIB (Hunter 2007) software package and the GNU Scientific Library (Galassi et al. 2009). This research has made use of NASA’s Astrophysics Data System.

## REFERENCES

- Abazajian K. N. et al., 2009, *ApJS*, 182, 543  
 Aihara H. et al., 2018, *PASJ*, 70, S4  
 Baldauf T., Smith R. E., Seljak U., Mandelbaum R., 2010, *Phys. Rev. D*, 81, 063531  
 Behroozi P. S., Wechsler R. H., Wu H.-Y., 2013, *ApJ*, 762, 109  
 Benson A. J., Cole S., Frenk C. S., Baugh C. M., Lacey C. G., 2000, *MNRAS*, 311, 793  
 Berlind A. A., Weinberg D. H., 2002, *ApJ*, 575, 587  
 Bond J. R., Cole S., Efstathiou G., Kaiser N., 1991, *ApJ*, 379, 440  
 Bryan G. L., Norman M. L., 1998, *ApJ*, 495, 80  
 Cacciato M., van den Bosch F. C., More S., Li R., Mo H. J., Yang X., 2009, *MNRAS*, 394, 929  
 Cacciato M., Lahav O., van den Bosch F. C., Hoekstra H., Dekel A., 2012, *MNRAS*, 426, 566  
 Cacciato M., van den Bosch F. C., More S., Mo H., Yang X., 2013, *MNRAS*, 430, 767  
 Center O. S., 1987, Ohio Supercomputer Center, <http://osc.edu/ark:/19495/f5s1ph73> (accessed January 14, 2019)  
 Cooray A., Hu W., 2001, *ApJ*, 554, 56  
 Correa C. A., Wyithe J. S. B., Schaye J., Duffy A. R., 2015, *MNRAS*, 452, 1217  
 Coupon J. et al., 2012, *A&A*, 542, A5  
 Dawson K. S. et al., 2013, *AJ*, 145, 10  
 Abbott T. M. C. et al., 2018, *Phys. Rev. D*, 98, 043526  
 Eisenstein D. J. et al., 2011, *AJ*, 142, 72  
 Elvin-Poole J. et al., 2018, *Phys. Rev. D*, 98, 042006  
 Galassi M., Davies J., Theiler J., Gough B., Jungman G., Alken P., Booth M., Rossi F., 2009, GNU Scientific Library Reference Manual. 3rd edn, Network Theory Ltd, United Kingdom  
 Gao L., Springel V., White S. D. M., 2005, *MNRAS*, 363, L66  
 Garrison L. H., Eisenstein D. J., Ferrer D., Metchnik M. V., Pinto P. A., 2016, *MNRAS*, 461, 4125  
 Garrison L. H., Eisenstein D. J., Ferrer D., Tinker J. L., Pinto P. A., Weinberg D. H., 2017, *ApJS*, 236, 43  
 Guo H. et al., 2014, *MNRAS*, 441, 2398  
 Harker G., Cole S., Helly J., Frenk C., Jenkins A., 2006, *MNRAS*, 367, 1039  
 Hearin A. P., Watson D. F., 2013, *MNRAS*, 435, 1313  
 Hearin A. P., Zentner A. R., van den Bosch F. C., Campbell D., Tollerud E., 2016, *MNRAS*, 460, 2552  
 Heitmann K., Higdon D., White M., Habib S., Williams B. J., Lawrence E., Wagner C., 2009, *ApJ*, 705, 156  
 Heymans C. et al., 2012, *MNRAS*, 427, 146  
 Hildebrandt H. et al., 2017, *MNRAS*, 465, 1454  
 Ho S., Lin Y.-T., Spergel D., Hirata C. M., 2009, *ApJ*, 697, 1358



- Hu W., Kravtsov A. V., 2003, *ApJ*, 584, 702
- Hunter J. D., 2007, *Comput. Sci. Eng.*, 9, 90
- Jain B., Seljak U., 1997, *ApJ*, 484, 560
- Jee M. J., Tyson J. A., Hilbert S., Schneider M. D., Schmidt S., Wittman D., 2016, *ApJ*, 824, 77
- Leauthaud A., Tinker J., Behroozi P. S., Busha M. T., Wechsler R. H., 2011, *ApJ*, 738, 45
- Leauthaud A. et al., 2017, *MNRAS*, 467, 3024
- Lehmann B. V., Mao Y.-Y., Becker M. R., Skillman S. W., Wechsler R. H., 2017, *ApJ*, 834, 37
- Lemson G., Kauffmann G., 1999, *MNRAS*, 302, 111
- Lewis A., Challinor A., 2011, Astrophysics Source Code Library, record ascl:1102.026
- Mandelbaum R. et al., 2005, *MNRAS*, 361, 1287
- Mandelbaum R., Seljak U., Cool R. J., Blanton M., Hirata C. M., Brinkmann J., 2006, *MNRAS*, 372, 758
- Mandelbaum R., Slosar A., Baldauf T., Seljak U., Hirata C. M., Nakajima R., Reyes R., Smith R. E., 2013, *MNRAS*, 432, 1544
- Marian L., Smith R. E., Angulo R. E., 2015, *MNRAS*, 451, 1418
- McEwen J. E., Weinberg D. H., 2018, *MNRAS*, 477, 4348
- Metchnik M. V. L., 2009, PhD thesis. The University of Arizona
- More S., 2013, *ApJ*, 777, L26
- More S., van den Bosch F. C., Cacciato M., More A., Mo H., Yang X., 2013, *MNRAS*, 430, 747
- More S., Miyatake H., Mandelbaum R., Takada M., Spergel D. N., Brownstein J. R., Schneider D. P., 2015, *ApJ*, 806, 2
- Murata R., Nishimichi T., Takada M., Miyatake H., Shirasaki M., More S., Takahashi R., Osato K., 2018, *ApJ*, 854, 120
- Navarro J. F., Frenk C. S., White S. D. M., 1997, *ApJ*, 490, 493
- Parejko J. K. et al., 2013, *MNRAS*, 429, 98
- Planck Collaboration (XIII), 2016, *A&A*, 594, A13
- Prat J. et al., 2018, *Phys. Rev. D*, 98, 042005
- Roza E. et al., 2016, *MNRAS*, 461, 1431
- Salcedo A. N., Maller A. H., Berlind A. A., Sinha M., McBride C. K., Behroozi P. S., Wechsler R. H., Weinberg D. H., 2018, *MNRAS*, 475, 4411
- Scoccimarro R., Zaldarriaga M., Hui L., 1999, *ApJ*, 527, 1
- Sheldon E. S. et al., 2004, *AJ*, 127, 2544
- Sheth R. K., Tormen G., 2004, *MNRAS*, 350, 1385
- Singh S., Mandelbaum R., Seljak U., Slosar A., Vazquez Gonzalez J., 2017, *MNRAS*, 471, 3827
- Sinha M., Garrison L., 2017, Astrophysics Source Code Library, record ascl:1703.003
- Tojeiro R. et al., 2014, *MNRAS*, 440, 2222
- Troxel M. A. et al., 2018, *Phys. Rev. D*, 98, 043528
- van Daalen M. P., Schaye J., McCarthy I. G., Booth C. M., Dalla Vecchia C., 2014, *MNRAS*, 440, 2997
- van den Bosch F. C., More S., Cacciato M., Mo H., Yang X., 2013, *MNRAS*, 430, 725
- Wechsler R. H., Zentner A. R., Bullock J. S., Kravtsov A. V., Allgood B., 2006, *ApJ*, 652, 17
- Weinberg D. H., Mortonson M. J., Eisenstein D. J., Hirata C., Riess A. G., Roza E., 2013, *Phys. Rep.*, 530, 87
- White S. D. M., 1994, preprint (arXiv)
- Yoo J., Seljak U., 2012, *Phys. Rev. D*, 86, 083504
- Yoo J., Tinker J. L., Weinberg D. H., Zheng Z., Katz N., Davé R., 2006, *ApJ*, 652, 26
- York D. G. et al., 2000, *AJ*, 120, 1579
- Zehavi I. et al., 2005, *ApJ*, 630, 1
- Zehavi I. et al., 2011, *ApJ*, 736, 59
- Zentner A. R., Hearin A. P., van den Bosch F. C., 2014, *MNRAS*, 443, 3044
- Zentner A. R., Hearin A., van den Bosch F. C., Lange J. U., Villarreal A., 2016, preprint (arXiv:1606.07817)
- Zheng Z., Guo H., 2016, *MNRAS*, 458, 4015
- Zheng Z. et al., 2005, *ApJ*, 633, 791
- Zu Y., Mandelbaum R., 2015, *MNRAS*, 454, 1161

## SUPPORTING INFORMATION

Supplementary data are available at [MNRAS](#) online.

### online\_only\_tables.tar.gz

Please note: Oxford University Press is not responsible for the content or functionality of any supporting materials supplied by the authors. Any queries (other than missing material) should be directed to the corresponding author for the article.

## APPENDIX A: ALTERNATIVE ESTIMATOR FOR GALAXY-GALAXY LENSING

On sufficiently large scales, the net impact of HOD parameters on  $\xi_{\text{gg}}$  and  $\xi_{\text{gm}}$  should be described by a scale-independent bias factor  $b_g$ . However, the derivatives of  $\gamma_t(r_p)$  with respect to some HOD parameters retain substantial scale-dependence even at  $r_p > 10 h^{-1}$  Mpc (Fig. 4) because  $\gamma_t$  remains sensitive to non-linear scales even when  $r_p$  is large (equation 11). The  $\Upsilon$  estimator of Baldauf et al. (2010) is designed to remove this sensitivity, effectively subtracting out information from small scales.

Fig. A1 compares HOD parameter derivatives for  $\gamma_t$  and  $\Upsilon$ , with the latter implemented for cut-off scales  $R_0 = 2$  and  $5 h^{-1}$  Mpc. For parameters  $\ln M_1/M_{\text{min}}$ ,  $\ln n_{\text{gal}}$ , and  $\ln \sigma_{\log M}$ , the  $\Upsilon$  estimator greatly reduces the scale-dependence of derivatives at large  $r_p$ , more completely for  $R_0 = 5 h^{-1}$  Mpc as expected. Derivatives with respect to  $Q_{\text{env}}$  remain mildly scale-dependent at  $r_p = 10 - 30 h^{-1}$  Mpc, because the  $8 h^{-1}$  Mpc scale used for defining the halo environment is itself fairly large.



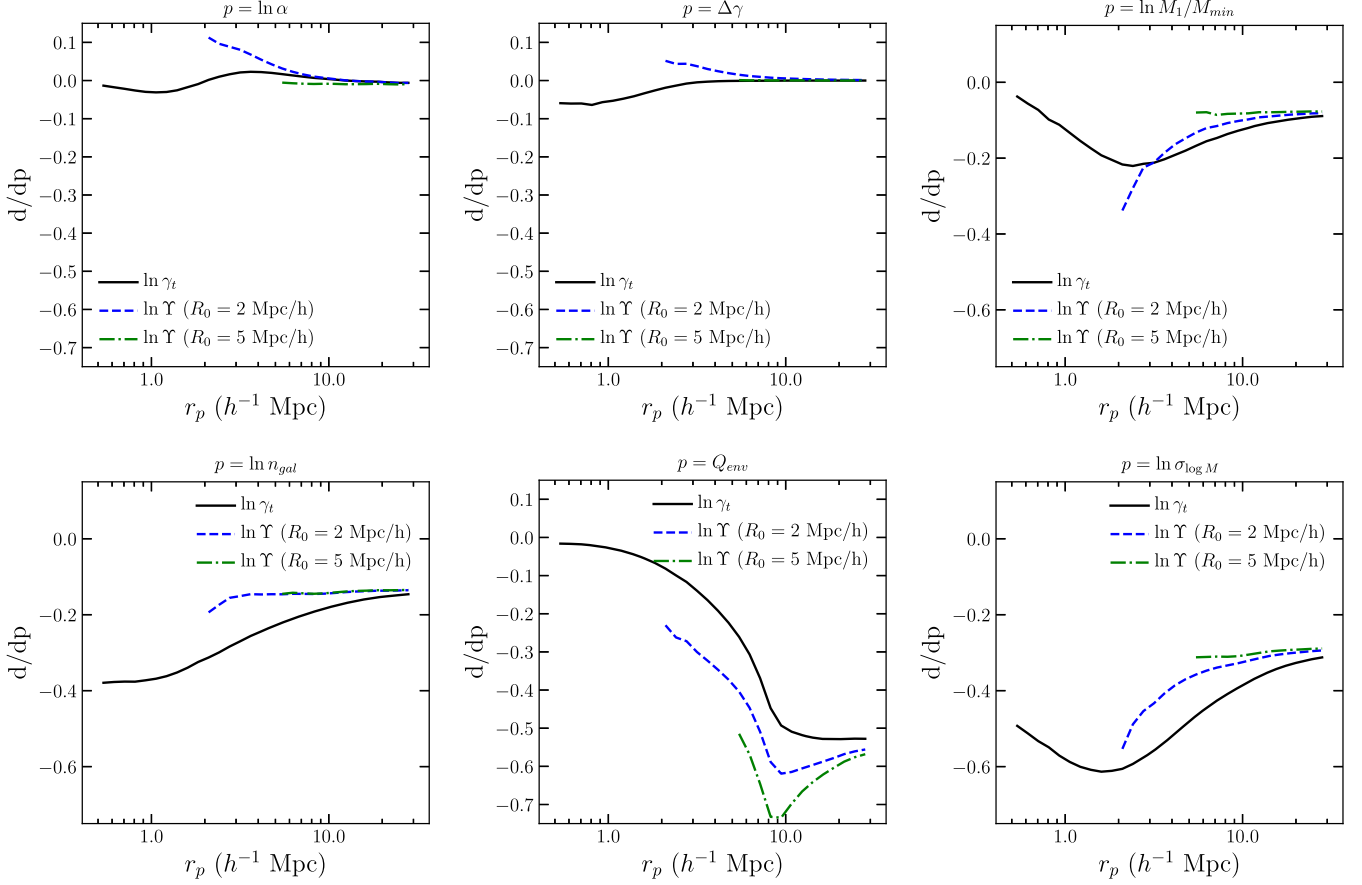


**Figure A1.** The logarithmic derivatives of various GGL estimators for various HOD parameters.

## APPENDIX B: EMULATOR DERIVATIVES

Table B1 lists the fiducial values and derivatives with respect to HOD and cosmological parameters of  $\ln b_g$  as a function of radial bin separation for the first 10 radial bins of the full table.

Table B2 lists the fiducial values and derivatives with respect to HOD and cosmological parameters of  $\ln r_{gm}$  as a function of radial bin separation for the first 10 bins. Table B3 lists the fiducial values and derivatives with respect to cosmological parameters of  $\ln b_{nl}$  for the first 10 bins. The full tables are provided as machine-readable ASCII tables in the online Supporting Information.

**Table B1.** Fiducial value and derivatives of  $\ln b_g$  with respect to HOD and cosmological parameters, as a function of radial bins  $[r_i, r_{i+1}]$ .

$r_i$	$r_{i+1}$	Fiducial	$\partial/\partial \ln n_{gal}$	$\partial/\partial \ln \sigma_{log M}$	$\partial/\partial \ln M_1/M_{min}$	$\partial/\partial \ln \alpha$	$\partial/\partial Q_{env}$	$\partial/\partial \Delta\gamma$	$\partial/\partial \ln \Omega_M$	$\partial/\partial \ln \sigma_8$
0.0100	0.0112	2.2492	0.6278	-1.0257	-2.5696	-1.2251	-0.0109	-1.7414	0.7138	-0.7489
0.0112	0.0126	1.9929	0.0409	-1.4647	-0.7558	-0.4214	0.0150	-1.4644	-0.5804	-0.7377
0.0126	0.0142	2.4367	-0.3515	-1.2786	-0.8185	-0.5352	-0.0059	-1.8984	0.6373	-0.4411
0.0142	0.0159	2.0490	0.0793	-1.6480	-0.3119	-0.8853	-0.0039	-1.4772	-0.6896	-0.4465
0.0159	0.0179	1.8773	-0.1103	-1.2147	0.1358	-0.7216	-0.0138	-1.6936	-0.3708	-0.7008
0.0179	0.0201	2.0060	0.4151	-1.0349	-0.6610	-0.8776	-0.0071	-1.3927	-1.1537	1.2640
0.0201	0.0226	2.0400	0.3419	-1.2712	-1.0811	-0.9839	-0.0001	-1.8048	0.6078	-0.8494
0.0226	0.0254	1.8421	0.2407	-1.5000	-0.8838	-0.9279	0.0098	-1.7163	0.1132	-0.6852
0.0254	0.0285	1.9109	-0.4028	-1.2632	-1.3304	-0.5197	0.0048	-1.2004	-0.0885	-0.6315
0.0285	0.0320	1.6828	0.2611	-1.5507	-0.6485	-0.6831	-0.0042	-1.1353	-0.2277	-1.4978

**Table B2.** Fiducial value and derivatives of  $\ln r_{\text{gm}}$  with respect to HOD and cosmological parameters, as a function of radial bins  $[r_i, r_{i+1}]$ .

$r_i$	$r_{i+1}$	Fiducial	$\partial/\partial \ln n_{\text{gal}}$	$\partial/\partial \ln \sigma_{\log M}$	$\partial/\partial \ln M_1/M_{\text{min}}$	$\partial/\partial \ln \alpha$	$\partial/\partial Q_{\text{env}}$	$\partial/\partial \Delta\gamma$	$\partial/\partial \ln \Omega_M$	$\partial/\partial \ln \sigma_8$
0.0100	0.0112	1.3997	-0.9873	0.7442	2.7071	1.2602	-0.0544	1.7170	-0.3676	2.7523
0.0112	0.0126	1.3034	-0.3727	1.1477	0.8599	0.4457	-0.0943	1.4648	1.1642	2.0329
0.0126	0.0142	1.8720	0.0087	0.9770	0.8789	0.5470	-0.0196	1.9009	-0.5359	2.2829
0.0142	0.0159	1.5348	-0.4251	1.3309	0.3753	0.9039	-0.0148	1.4800	1.0433	1.9450
0.0159	0.0179	1.4248	-0.2047	0.8868	-0.0684	0.7426	0.0067	1.6820	-0.1445	1.5945
0.0179	0.0201	1.6686	-0.7059	0.7138	0.7167	0.9001	-0.0428	1.3826	-0.7254	0.2783
0.0201	0.0226	1.7257	-0.6624	0.9647	1.1101	1.0167	-0.0140	1.7922	-0.0107	0.8995
0.0226	0.0254	1.6475	-0.5777	1.1906	0.9388	0.9686	-0.0239	1.6915	0.2043	0.5866
0.0254	0.0285	1.6799	0.0792	0.9562	1.3640	0.5474	-0.0454	1.1910	0.1123	-0.8946
0.0285	0.0320	1.6269	-0.5976	1.2445	0.6959	0.7063	-0.0243	1.1251	-0.0225	-0.3697

**Table B3.** Fiducial value and derivatives of  $\ln b_{\text{nl}}$  with respect to HOD and cosmological parameters, as a function of radial bins  $[r_i, r_{i+1}]$ .

$r_i$	$r_{i+1}$	Fiducial	$\partial/\partial \ln \sigma_8$	$\partial/\partial \ln \Omega_M$
0.0100	0.0112	1.3277	-0.4060	-0.1488
0.0112	0.0126	1.4792	-0.2433	0.1631
0.0126	0.0142	1.0111	-1.0000	-0.5412
0.0142	0.0159	1.3407	-0.7627	-0.2355
0.0159	0.0179	1.4737	-0.1833	0.2402
0.0179	0.0201	1.2782	-1.1902	0.4009
0.0201	0.0226	1.2126	0.3140	-0.7944
0.0226	0.0254	1.3546	-0.0298	-0.2946
0.0254	0.0285	1.2875	0.2068	-0.2943
0.0285	0.0320	1.4277	0.7104	0.0258

This paper has been typeset from a  $\text{\TeX}/\text{\LaTeX}$  file prepared by the author.